Le fond extragalactique infrarouge

Sommaire

5.1 Contribution totale des galaxies infrarouges au fond extragalactique

Chap. 2, 3 et 4, nous avons déterminé par des méthodes variées les comptages de galaxies infrarouges à différentes longueurs d'onde infrarouges et sub-millimétriques. A partir de

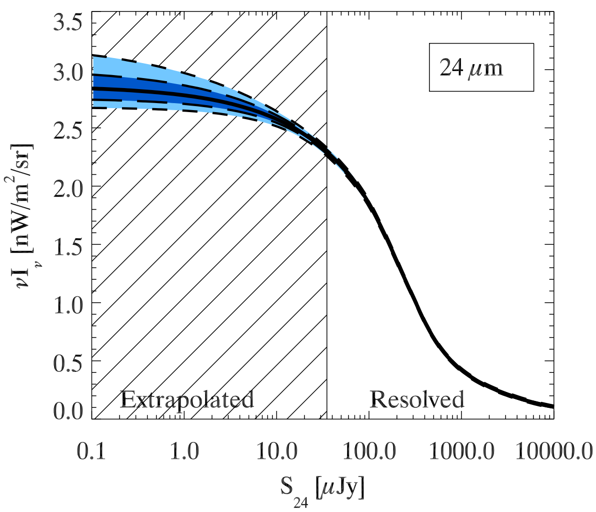

FIGURE 5.1 – Contribution cumulée au fond infrarouge à 24 μm en fonction du flux. Les deux zones colorées correspondent à 1 et 2-σ. Extrait de Béthermin *et al.* (2010a).

ceux-ci, il est facile d'estimer la contribution des sources infrarouges au fond infrarouge B :

$$B = \int S \frac{dN}{dS} dS. \tag{5.1}$$

Ceci fournit des limites inférieures sur le niveau du fond infrarouge qui peuvent être comparées avec les mesures absolues et les limites supérieures.

5.1.1 Fond infrarouge à 24 μm

Des comptages profonds à 24 μm ont été estimés Sect. 2.5.3. On peut, à partir de cela, calculer grâce à l'Eq. 5.1 comment les sources contribuent au fond infrarouge à 24 μm. La contribution des sources situées dans l'intervalle de flux étudié (35 μJy< S_{24} <100 mJy) par nos comptages est 2.26±0.09 nW.m^{-2}.sr^{-1}. La contribution des sources plus brillantes que notre plus haut bin de flux est négligeable 0.032±0.003 nW.m^{-2}.sr^{-1} (on extrapole ici un comportement euclidien). En revanche, la contribution des sources faibles ne l'est pas. A bas flux, les comptages ont en un comportement en loi de puissance (dN/dS$\propto S^{-1.45\pm0.1}$). On peut alors extrapoler ce comportement jusqu'à flux nul pour estimer la contribution totale des galaxies au fond infrarouge : $2.86^{+0.19}_{-0.16}$ nW.m^{-2}.sr^{-1}. Les incertitudes sont réduites d'un facteur 5 environ par rapport aux estimations précédentes de Papovich *et al.* (2004) à partir des comptages *Spitzer* du temps garanti. Ces estimations sont également en accord avec les limites supérieures provenant de rayons gamma (5 nW.m^{-2}.sr^{-1}, Mazin et Raue (2007)). La Fig. 5.1 illustre la contribution cumulée des sources en fonction du flux.

Les sources résolues à 24 μm expliquent donc 80% du fond total extrapolé. Si on considère que les galaxies sont la seule source d'émission du fond infrarouge à cette longueur d'onde, on peut donc considérer que le fond est quasiment résolu dans l'infrarouge moyen. Néanmoins, il n'existe pas de mesure absolue à cette longueur d'onde pour tester cette hypothèse. En effet, la lumière zodiacale domine de trois ordres de grandeur le fond extragalactique dans cette partie du spectre. Ces contributions pourraient être dues à une émission diffuse du milieu intergalactique (Montier et Giard (2005)) ou d'une contribution de sources ponctuelles très faibles telle que les étoiles de populations III (Raue *et al.* (2009)).

5.1.2 Fond infrarouge à 70 et 160 μm

La contribution des sources résolues à 70 (S_{70} >3.5 mJy) et 160 μm (S_{160} >40 mJy) au fond infrarouge est de 3.1±0.2 nW.m^{-2}.sr^{-1} et 1.0±0.1 nW.m^{-2}.sr^{-1}, respectivement (calculé à partir des comptages présentés Sect. 2.5.3). Si on ajoute la contribution des sources sondées par la méthode de l'empilement (voir Sect. 3.2.3), on a alors 5.4±0.4 nW.m^{-2}.sr^{-1} et 8.9±1.1 nW.m^{-2}.sr^{-1}, respectivement. L'empilement est donc crucial pour sonder les sources responsables du fond à 160 μm. De plus, les comptages par empilement permettent de déterminer la pente des comptages à bas flux, et d'extrapoler la contribution totale des galaxies au fond. On trouve alors une contribution totale de $6.6^{+0.7}_{-0.6}$ nW.m^{-2}.sr^{-1} et $14.6^{+7.1}_{-2.9}$ nW.m^{-2}.sr^{-1}, respectivement. La Fig. 5.2 montre la contribution cumulée au fond dans ces deux bandes. Cette dernière valeur est en accord avec la mesure absolue de Pénin *et al.* (2011b) : 14.4±3 nW.m^{-2}.sr^{-1}. L'hypothèse d'un fond dû uniquement aux galaxies est donc compatible avec les observations actuelles. Néanmoins, les larges incertitudes de mesure laissent de la place pour d'éventuelles autres composantes non négligeables.

5.1.3 Fond infrarouge dans le domaine sub-millimétrique

Au delà de 200 μm, le niveau du fond infrarouge a été mesuré avec précision par FIRAS (Lagache *et al.* (2000)). Il est donc facile d'estimer la fraction du fond résolue par les différents comptages. La Fig. 5.3 présente la contribution au fond en fonction du flux de coupure des comptages. Les sources résolues par BLAST ne sont à l'origine que d'une infime partie du fond infrarouge à 250, 350 et 500 μm (2.3%, 1.1% et 0.4%, respectivement, Béthermin *et al.* (2010b)). Grâce à la meilleur résolution angulaire de SPIRE, Oliver *et al.* (2010) résolvent directement 15%, 10% et 6% du fond, respectivement. Pour aller plus

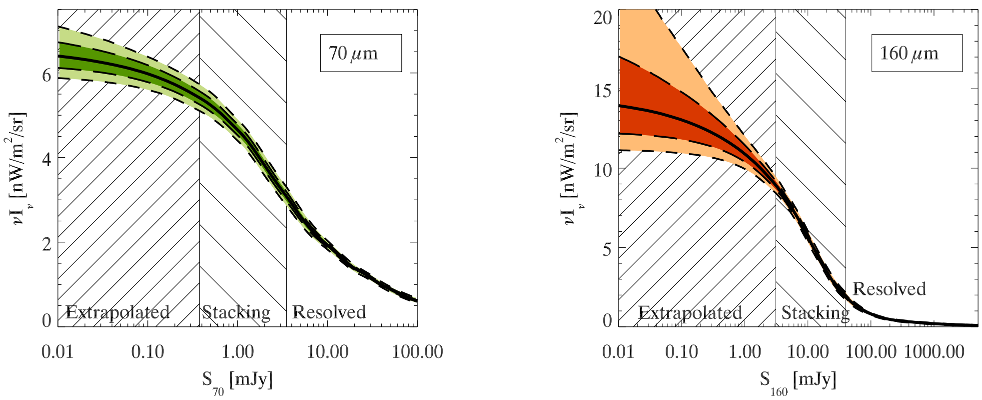

FIGURE 5.2 – Contribution cumulée au fond infrarouge à 70 (gauche) et 160 μm (droite) en fonction du flux. Les deux zones colorées correspondent à 1 et 2-σ. Extrait de Béthermin *et al.* (2010a).

loin, il faut faire appel à l'analyse par empilement des données BLAST, qui resout environ 50% du fond. Dans le cas de l'analyse P(D), on ne peut pas parler directement de fraction résolue. En effet, l'analyse P(D) analyse tout les régimes de flux simultanément. On peut également forcer le résultat à être en accord avec la mesure du fond total. Nous avons ici comparé le modèle spline avec a priori FIRAS aux autres estimations de la contribution différentielle au fond. Dans tout les cas, il y a un très bon accord entre le modèle P(D) et les autre mesures.

5.1.4 Conclusion

Les sources résolues par *Spitzer* et BLAST ne résolvent qu'une faible fraction du fond au delà de 70 μm. En revanche, la méthode de l'empilement permet en revanche de produire des comptages suffisamment profonds pour qu'ils suffisent à expliquer l'origine du fond infrarouge à 70 et 160 μm. A plus grande longueur d'onde, les données BLAST ne permettent pas de mesurer la pente des comptages à bas flux afin de l'extrapoler. Les données *Herschel* devraient permettre, dans un futur proche, de mesurer avec une bien meilleure précision les comptages dans ce domaine de longueur d'onde.

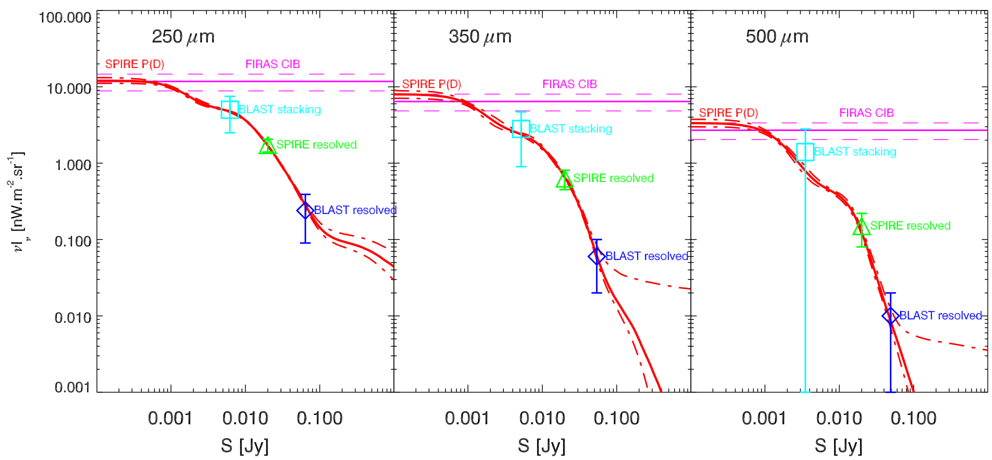

FIGURE 5.3 – Contribution cumulée au fond infrarouge à 250 (gauche), 350 (milieu) et 500 μm (droite) en fonction du flux. (Lignes violette) : Niveau absolu du fond mesuré par FIRAS (Lagache *et al.* (2000)), et zone de confiance à 1σ. (Lignes rouges) : contribution des comptages P(D) SPIRE (modèle spline avec a priori FIRAS, Glenn *et al.* (2010)). (Losange bleu) : contribution des sources BLAST résolues (Béthermin *et al.* (2010b)). (Triangle vert) : contribution des sources SPIRE résolues (Oliver *et al.* (2010)). (Carré bleu ciel) : contribution des sources BLAST mesurée par empilement (Béthermin *et al.* (2010b)).

5.2 Contribution des sources détectées par *Spitzer* à 24 μm au fond infrarouge et au taux formation d'étoiles en fonction du *redshift*

Les travaux présentés dans cette partie ont été réalisés en collaboration avec Joaquin Vieira et HerMES (programme de temps garanti SPIRE). Un article est en cours de préparation.

Dans certains champs profonds comme GOODS ou COSMOS, les sources infrarouges à 24 μm peuvent être en général associées à des sources optiques dont le *redshift* est connu. On peut, par exemple, réaliser une extraction de sources en prenant la position des sources optiques comme *a priori* (Magnelli *et al.* (2009)). Il est également possible d'utiliser un catalogue infrarouge extrait en aveugle et de rechercher les sources optiques les plus proches pour réaliser l'identification (par exemple, Le Floc'h *et al.* (2009)). Pour les sources brillantes en optique, le *redshift* est estimé directement à partir du spectre haute résolution, en mesurant le décalage des raies. Dans ce cas la mesure est, en général, très précise. On parle alors de *redshifts* spectroscopiques. Dans la majorité des cas, le spectre des objets n'est pas accessible (manque de temps de télescope, objet trop faible en optique...). Il est alors possible d'estimer le *redshift* en ajustant des *templates* de SED aux points photométriques obtenus en bande large. Cette méthode permet d'associer un *redshift* à quasiment toutes les sources infrarouges détectées. Toutefois, ces *redshifts* "photométriques" sont beaucoup moins précis que les *redshifts* spectroscopiques ($\sigma_z \sim 10^{-3}$ pour les *redshifts* spectroscopiques de Lilly *et al.* (2007), contre $\sigma_z \sim 10^{-2}$ à 10^{-1} pour les *redshifts* photométriques de Ilbert *et al.* (2009)).

Dans les champs où le *redshift* de la quasi-totalité des sources 24 μm est disponible, il est possible d'empiler toutes les sources 24 μm d'une fine tranche de *redshift* afin de déterminer leur émission totale dans l'infrarouge lointain et le domaine sub-millimétrique. Ceci permet d'obtenir des contraintes fortes sur les modèles d'évolution, mais également de placer des limites inférieures sur le taux de formation d'étoiles à haut *redshift*. Ces mesures devraient également permettre d'améliorer les modèle d'absorption des rayons γ par le fond infrarouge.

5.2.1 Contribution des sources 24 μm au fond infrarouge à plus grande longueur d'onde

La contribution différentielle des sources infrarouges au fond en fonction du *redshift*, dB/dz, se calcule en divisant la contribution d'une tranche de *redshift* ΔB par la taille Δz de celle-ci. Toutefois, il est impossible de mesurer directement la contribution totale

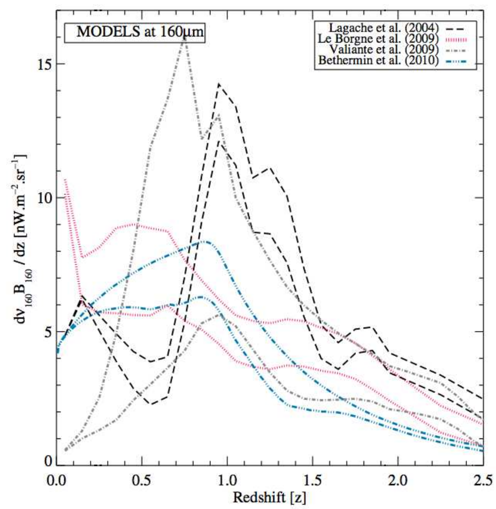

FIGURE 5.4 – Distribution en *redshift* du fond infrarouge à 160 μm pour les modèles de Lagache *et al.* (2004) (en noir), Le Borgne *et al.* (2009) (en rouge), Valiante *et al.* (2009) (en gris) et de Béthermin *et al.* (2011) (en bleu). Pour chaque modèle deux courbes sont tracées : celle du bas correspond à la contribution des sources $S_{24} > 80$ μJy et celle du haut au fond total. Cette figure est tirée de Jauzac *et al.* (2011).

d'une tranche, mais on peut estimer une limite inférieure sur celle-ci en sommant l'émission des sources résolues. Dans l'infrarouge lointain, seule une faible fraction du fond est résolue en sources. Une limite inférieure plus contraignante peut alors être estimée par empilement des sources détectées à 24 μm. La Fig. 5.4 compare la contribution différentielle totale au fond infrarouge et celle des sources détectées à 24 μm uniquement pour différents modèles. Elle montre que les deux distributions ont des formes similaires, et que ces limites inférieures sont assez proches de la valeur totale (au plus 50 % inférieures au fond total, et souvent moins de 20% inférieures au total). Ces mesure permettent donc de contraindre fortement l'histoire du fond infrarouge.

J'ai collaboré à la première mesure de la contribution différentielle des sources détectées à 24 μm au fond à 70 et 160 μm par empilement de Jauzac *et al.* (2011). Cette mesure a été réalisée à partir des cartes *Spitzer* du champ COSMOS et du catalogue de sources à 24 μm associé à leur *redshift* de Le Floc'h *et al.* (2009). J'ai ensuite réalisé cette même mesure dans le champ GOODS-N en utilisant à la fois les données MIPS, SPIRE et AzTEC, ainsi qu'un catalogue d'entrée (flux à 24 μm et *redshift*) construit par Joaquin Vieira (Vieira *et al.*, en préparation). Cette mesure a été réalisée en utilisant la méthode d'empilement de Marsden *et al.* (2009) sans lissage préalable des cartes et la méthode du *bootstrap* pour déterminer les incertitudes de mesures. Le biais dû au regroupement est estimé à partir d'une simulation où la position des sources et leur flux 24 μm sont les

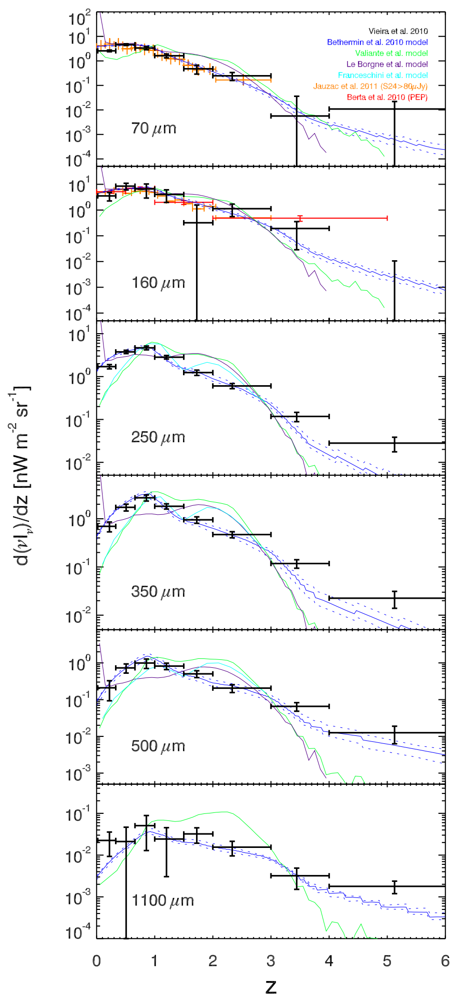

FIGURE 5.5 – Contribution différentielle des sources détectées à 24 μm au fond infrarouge à 70, 160, 250, 350 et 500 μm. *En noir :* résultat obtenu par empilement des sources S_{24} >40 μJy dans les cartes *Spitzer* (70 et 160 μm) et *Herschel* (250, 350 et 500 μm) du champ GOODS-N. *En orange :* résultat obtenu par empilement des sources S_{24} >80 μJy dans les cartes *Spitzer* du champ COSMOS (Jauzac *et al.* (2011)). *En rouge :* Distribution des sources résolues par l'instrument PACS à 160 μm (Berta *et al.* (2010)). Les lignes pleines représentent les modèles d'évolution de Béthermin *et al.* (2011) (bleu marine), Valiante *et al.* (2009) (vert), Le Borgne *et al.* (2009) (violet) et de Franceschini *et al.* (2010) (bleu ciel).

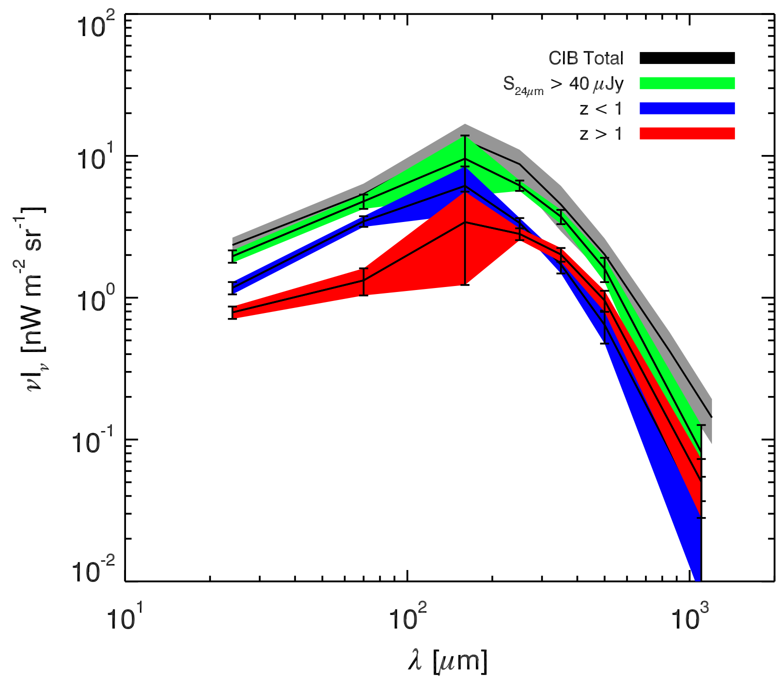

FIGURE 5.6 – Distribution spectrale d'énergie du fond infrarouge. *En noir :* fond total. *En vert :* contribution des sources à 24 μm. *En bleu* : contribution des sources à 24 μm à bas *redshift* (z<1.2). *En rouge* : contribution des sources à 24 μm à bas *redshift* (z>1.2)

mêmes que dans les cartes réelles et où le flux dans l'infrarouge lointain est déterminé en multipliant le flux 24 μm par la couleur moyenne des sources dans la tranche de *redshift* associée. Nous avons estimé un biais de 7, 20, 6, 7, 11 et 11% à respectivement 70, 160, 250, 350, 500 et 1100 μm. La Fig. 5.5 montre les résultats obtenus. On observe une forte cassure à z$\sim$1. De plus, comme attendu, la contribution relative des hauts (resp. bas) *redshift* augmente (resp. diminue) quand la longueur d'onde augmente. Ces observations sont également très discriminantes pour les modèles d'évolution : en effet, un seul modèle parvient à reproduire globalement ces observations. Il s'agit du modèle que j'ai développé pendant ma thèse, et qui est présenté Chap. 6.

On peut également étudier la SED du CIB en séparant haut (z>1.2) et bas (z<1.2) *redshift*. La Fig. 5.8 représente ces différentes contributions. L'estimation du fond total est issue de FIRAS (Lagache *et al.* (2000)) au delà de 250 μm. A plus courte longueur d'onde, nous utilisons ma valeur totale extrapolée à partir des comptages à 70 μm (Béthermin *et al.* (2010a)), et la mesure absolue de Pénin *et al.* (2011b) à 160 μm. La contribution des sources détectées à 24 μm (S_{24} >40 μJy) est en bon accord avec les mesures de Dole *et al.* (2006) et mes propres mesures dans les bandes MIPS. En revanche, les valeurs dans les bandes SPIRE sont environ 20% inférieures à celle mesurée par Marsden *et al.* (2009). Cette différence s'explique, d'une part, par leur coupure du catalogue à 24 μm à 20 μJy (avec les risques de biais que comporte l'utilisation d'un catalogue comportant de nombreuses fausses détections), et d'autre part par un *beam* deux fois plus large et donc un plus fort biais dû au regroupement. Nous avons également utilisé les données AzTEC à 1.1 mm de Chapin *et al.* (2009b) pour prolonger la SED de l'EBL dans le domaine millimétrique. La séparation entre haut et bas *redshift* illustre le fait que plus on va à grande longueur d'onde et plus la contribution des grands *redshifts* est grande.

5.2.2 Distribution spectrale d'énergie moyenne de sources sélectionnées à 24 μm

Grâce à la méthode de l'empilement, il est possible de construire la SED moyenne dans l'infrarouge de galaxies sélectionnées à 24 μm, et qui ne sont pas détectables individuellement à grande longueur d'onde. La Fig. 5.7 montre la SED moyenne des sources 24 μ séparées en différentes tranches de *redshift* (z<0.33, 0.33<z<0.66, 1<z<1.5, 1.5<z<2, 2<z<3, 3<z<4, z>4). Nous avons estimé la luminosité infrarouge totale et la température de poussière en ajustant les mesures par le modèle suivant :

- Un corps noir modifié d'émissivité β=1.5 fixée aux grandes longueurs d'onde ($\lambda > \lambda_c$),
- Un comportement en loi de puissance d'exposant fixé $\alpha = 1.8$ aux courtes longueurs d'onde ($\lambda < \lambda_c$),

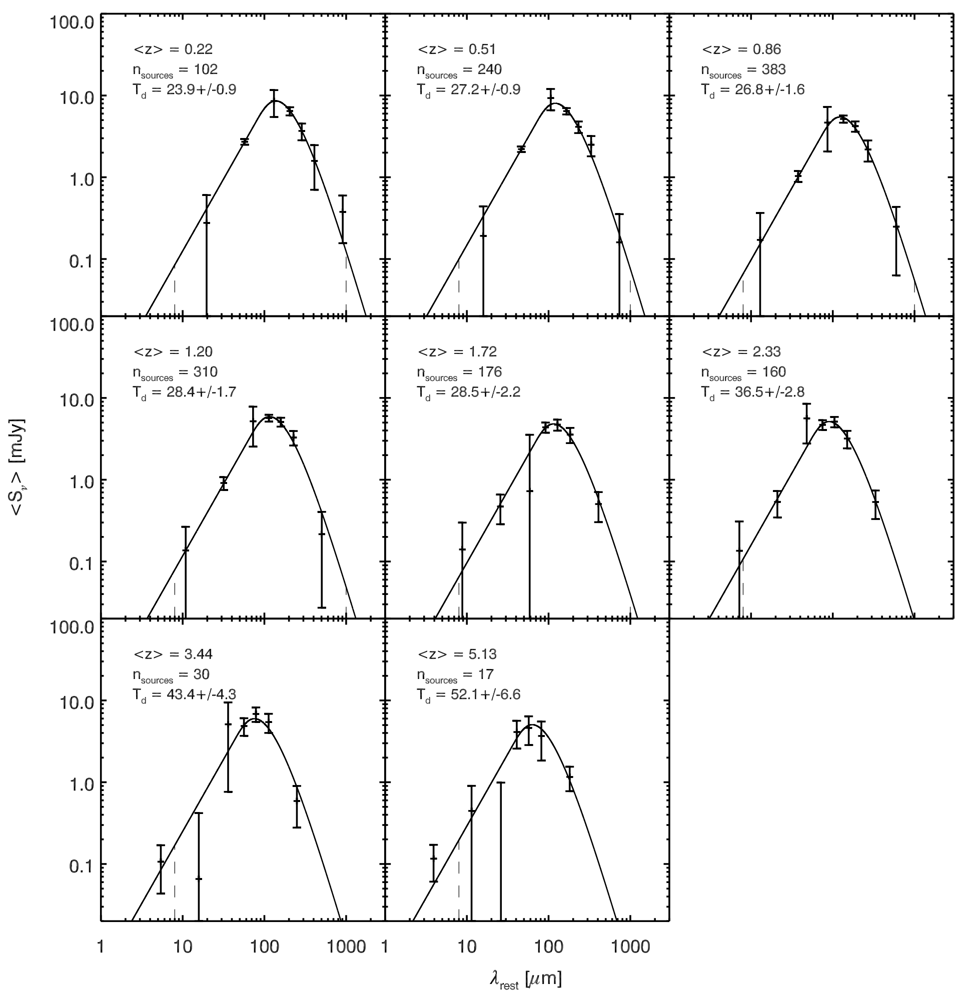

FIGURE 5.7 – Distribution spectrale d'énergie moyenne des galaxies sélectionnées à 24 μm (S_{24} >40 μJy) pour différentes tranches de *redshift* (z<0.33, 0.33<z<0.66, 1<z<1.5, 1.5<z<2, 2<z<3, 3<z<4, z>4).

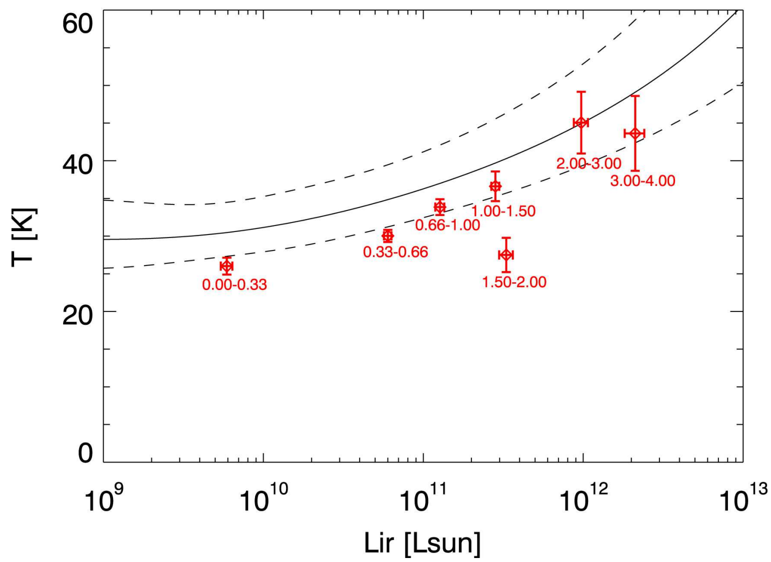

FIGURE 5.8 – Température en fonction de la luminosité des SED moyennes correspondant aux différentes tranches de *redshift* (*cercles rouges*), comparée avec la relation locale et sa dispersion mesurée par IRAS de Chapin *et al.* (2009a) (*ligne continue et pointillée*).

- On impose une continuité de la SED et de sa pente pour raccorder les deux parties. Cette condition fixe la valeur de λ_c.

En utilisant des *templates* de galaxies, nous avons montré que cette méthode simple permet de retrouver la luminosité infrarouge avec une précision de l'ordre de 10%, qui est bien inférieure aux erreurs statistiques. Les températures et luminosités moyennes trouvées suivent la relation locale entre luminosité et température mesurée par Chapin *et al.* (2009a). Ceci suggère donc une faible évolution de cette relation avec le *redshift*. Or, les températures des galaxies sélectionnées dans le domaine sub-millimétrique ont tendance à être plus froides que leurs analogues locaux. Le résultat trouvé par empilement suggère que ce phénomène est dû en partie à un biais de sélection.

5.2.3 Contribution des sources à 24 μm à la densité de luminosité infrarouge

A partir de la luminosité bolométrique infrarouge moyenne des sources 24 μm déterminée par empilement, il est possible de placer une limite inférieure sur la densité de luminosité infrarouge. Cette quantité est proportionnelle au taux de formation d'étoiles (Kennicutt (1998)), et est donc fondamentale pour comprendre l'histoire de la formation d'étoile. La méthode permettant de déterminer la densité de luminosité infrarouge dans une tranche de *redshift* consiste à calculer la luminosité totale produite par toute les sources 24 μm du

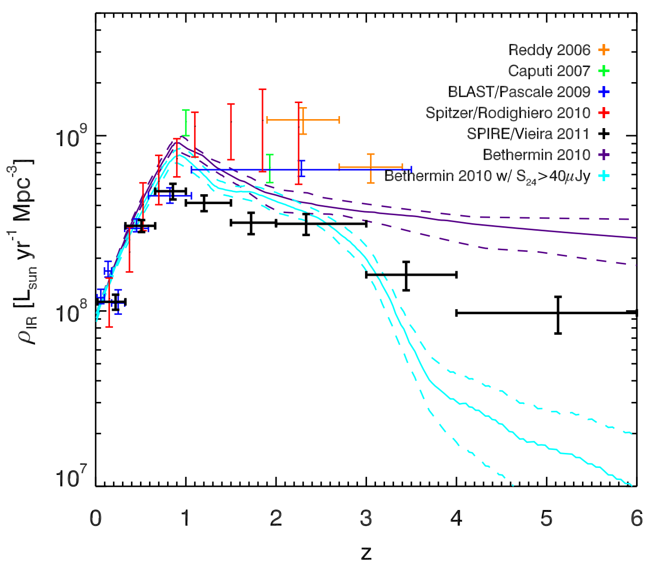

FIGURE 5.9 – Densité de luminosité infrarouge en fonction du *redshift*. *En noir :* contribution de toutes les sources 24 μm. Il s'agit d'une limite inférieure à la densité de luminosité totale. *En violet :* mesure de Reddy *et al.* (2008) à partir de l'UV. *En vert :* mesure à partir de la LF de Caputi *et al.* (2007) à partir du 24 μm *Spitzer*. *En bleu :* limite inférieure à partir de l'empilement des sources 24 μm dans les données BLAST de Pascale *et al.* (2009). *En violet :* prédiction de la densité de luminosité infrarouge totale par le modèle de Béthermin *et al.* (2011). *En bleu ciel :* prédiction de la contribution des sources 24 μm par le même modèle.

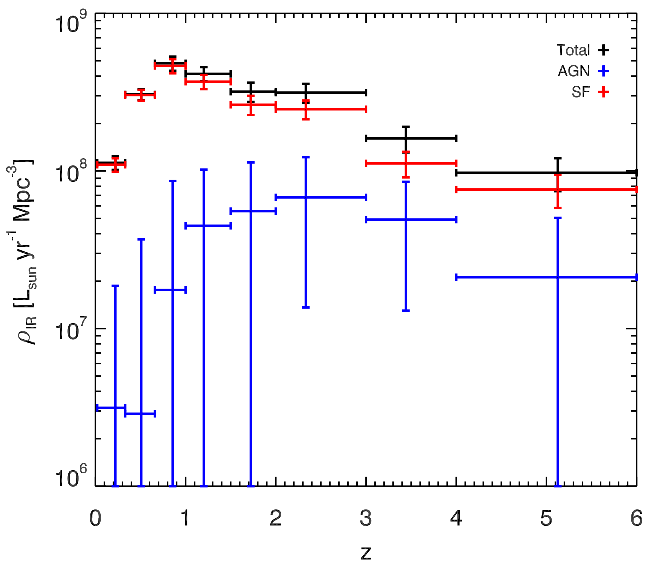

FIGURE 5.10 – Densité de luminosité infrarouge en fonction du *redshift*. *En noir :* Contribution de toutes les sources 24 μm. *En rouge :* Contribution des sources 24 μm dominée par la formation d'étoiles. *En noir :* Contribution des sources 24 μm dominée par leur noyau actif.

champ, et à la diviser par le volume comobile associé

$$V_c = \frac{\Omega}{3}\left(D_C(z_{max})^3 - D_C(z_{min})^3\right), \tag{5.2}$$

où Ω est la taille du champ utilisé, $D_C(z_{max})$ la distance comobile correspondant au *redshift* maximum de la tranche, z_{min} correspondant au *redshift* minimal de la tranche.

La Fig. 5.9 montre les résultats obtenus, et les compare avec les mesures précédentes. Nos limites inférieures augmentent jusqu'à z=1, puis diminuent. Cette diminution est due à la fois au fait que le 24 μm ne permet pas d'accéder aux faibles luminosités à haut *redshift*, mais aussi très probablement à une décroissance de la densité de luminosité infrarouge avec le *redshift* pour z> 1. Nos limites inférieures sont très proches des valeurs totales mesurées jusqu'à z=1. Au delà, elle sont significativement inférieures, le 24 μm ne sondant que les objets les plus brillants. On peut également comparer ces mesures avec les prédictions du modèle de Béthermin *et al.* (2011). La ligne bleu ciel représente une prédiction prenant en compte la sélection à 24 μm. L'accord est relativement bon, à l'exception d'une surestimation de 2σ à z~1, et à z>3. Il faut toutefois noter qu'au delà de z=3, le 24 μm observé ne sonde plus vraiment l'émission de la poussière, mais plutôt les vieilles populations stellaires qui ne sont pas modélisées avec précision. Nous avons également étudié la contribution des sources AGN, en les sélectionnant à partir de leur émission X. La Fig. 5.10 représente la contribution des sources AGNs et non-AGNs. On constate que cette contribution reste faible à tout *redshift*, et que la densité de luminosité infrarouge est donc toujours dominée par la formation d'étoiles.

5.2.4 Conclusion

Nous avons montré que l'empilement de sources sélectionnées en flux à 24 μm et en *redshift* fournit des contraintes très discriminantes sur l'évolution statistique des populations infrarouges. Ceci permet d'accéder à la distribution en *redshift* du fond infrarouge aux différentes longueurs d'onde, et ainsi de fournir de contraintes fortes sur le budget de photons que peuvent produire les processus de formation d'étoiles. Nos résultats indique que le taux de formation d'étoiles mesuré dans l'infrarouge augmente rapidement de z=0 à z=1. Le comportement à plus haut *redshift* semble plus stable, mais de grandes incertitudes sont encore présentes aujourd'hui, les populations de galaxies faibles ne pouvant pas être sondées, même par empilement.

5.3 Article : *Spitzer deep and wide legacy mid- and far-infrared number counts and lower limits of cosmic infrared background*

Les résultats présentés Chap. 2, 3 et 5 et concernant les comptages de sources et le CIB dans les bandes MIPS ont été publiés dans le journal *Astronomy&Astrophysics*.

A&A 512, A78 (2010)
DOI: 10.1051/0004-6361/200913279

Astronomy & Astrophysics

Spitzer deep and wide legacy mid- and far-infrared number counts and lower limits of cosmic infrared background*

M. Béthermin[1], H. Dole[1], A. Beelen[1], and H. Aussel[2]

[1] Institut d'Astrophysique Spatiale (IAS), Bt. 121, 91405 Orsay, France; Université Paris-Sud 11 and CNRS (UMR8617)
e-mail: mattieu.bethermin@ias.u-psud.fr
[2] Laboratoire AIM, CEA/DSM-CNRS-Université Paris Diderot, IRFU/Service d'Astrophysique, Bt. 709, CEA-Saclay, 91191 Gif-sur-Yvette Cedex, France

Received 11 September 2009 / Accepted 5 January 2010

ABSTRACT

Aims. We aim to place stronger lower limits on the cosmic infrared background (CIB) brightness at 24 μm, 70 μm and 160 μm and measure the extragalactic number counts at these wavelengths in a homogeneous way from various surveys.
Methods. Using *Spitzer* legacy data over 53.6 deg^2 of various depths, we build catalogs with the same extraction method at each wavelength. Completeness and photometric accuracy are estimated with Monte-Carlo simulations. Number count uncertainties are estimated with a counts-in-cells moment method to take galaxy clustering into account. Furthermore, we use a stacking analysis to estimate number counts of sources not detected at 70 μm and 160 μm. This method is validated by simulations. The integration of the number counts gives new CIB lower limits.
Results. Number counts reach 35 μJy, 3.5 mJy and 40 mJy at 24 μm, 70 μm, and 160 μm, respectively. We reach deeper flux densities of 0.38 mJy at 70, and 3.1 at 160 μm with a stacking analysis. We confirm the number count turnover at 24 μm and 70 μm, and observe it for the first time at 160 μm at about 20 mJy, together with a power-law behavior below 10 mJy. These mid- and far-infrared counts: 1) are homogeneously built by combining fields of different depths and sizes, providing a legacy over about three orders of magnitude in flux density; 2) are the deepest to date at 70 μm and 160 μm; 3) agree with previously published results in the common measured flux density range; 4) globally agree with the Lagache et al. (2004) model, except at 160 μm, where the model slightly overestimates the counts around 20 and 200 mJy.
Conclusions. These counts are integrated to estimate new CIB firm lower limits of $2.29^{+0.09}_{-0.09}$ nW m^{-2} sr^{-1}, $5.4^{+0.4}_{-0.4}$ nW m^{-2} sr^{-1}, and $8.9^{+1.1}_{-1.1}$ nW m^{-2} sr^{-1} at 24 μm, 70 μm, and 160 μm, respectively, and extrapolated to give new estimates of the CIB due to galaxies of $2.86^{+0.19}_{-0.16}$ nW m^{-2} sr^{-1}, $6.6^{+0.7}_{-0.6}$ nW m^{-2} sr^{-1}, and $14.6^{+7.1}_{-2.9}$ nW m^{-2} sr^{-1}, respectively. Products (point spread function, counts, CIB contributions, software) are publicly available for download at http://www.ias.u-psud.fr/irgalaxies/

Key words. cosmology: observations – diffuse radiation – galaxies: statistics – galaxies: evolution – galaxies: photometry – infrared: galaxies

1. Introduction

The extragalactic background light (EBL) is the relic emission of all processes of structure formation in the Universe. About half of this emission, called the Cosmic Infrared Background (CIB) is emitted in the 8–1000 μm range, and peaks around 150 μm. It is essentially due to the star formation (Puget et al. 1996; Fixsen et al. 1998; Hauser et al. 1998; Lagache et al. 1999; Gispert et al. 2000; Hauser & Dwek 2001; Kashlinsky 2005; Lagache et al. 2005).

The CIB spectral energy distribution (SED) is an important constraint for the infrared galaxies evolution models (e.g. Lagache et al. 2004; Franceschini et al. 2010; Le Borgne et al. 2009; Pearson & Khan 2009; Rowan-Robinson 2009; Valiante et al. 2009). It gives the budget of infrared emission since the first star. The distribution of the flux of sources responsible for this background is also a critical constraint. We propose to measure the level of the CIB and the flux distribution of the sources at 3 wavelengths (24 μm, 70 μm and 160 μm).

* Counts and CIB contributions are only available in electronic form at the CDS via anonymous ftp to cdsarc.u-strasbg.fr (130.79.128.5) or via http://cdsweb.u-strasbg.fr/cgi-bin/qcat?J/A+A/512/A78

In the 1980's, the infrared astronomical satellite (IRAS) and COBE/DIRBE performed the first mid-infrared (MIR) and far-infrared (FIR) full-sky surveys. Nevertheless, the detected sources were responsible for a very small part of the CIB. Between 1995 and 1998, the ISO (infrared space observatory) performed deeper observations of infrared galaxies. Elbaz et al. (2002) resolved into the source more than half of the CIB at 15 μm. At larger wavelengths, the sensitivity and angular resolution was not sufficient to resolve the CIB (Dole et al. 2001).

The *Spitzer* space telescope (Werner et al. 2004), launched in 2003, has performed deep infrared observations on wide fields. The multiband imaging photometers for *Spitzer* (MIPS) (Rieke et al. 2004) mapped the sky at 24 μm, 70 μm and 160 μm. About 60% of the CIB was resolved at 24 μm (Papovich et al. 2004) and at 70 μm (Frayer et al. 2006). Because of confusion (Dole et al. 2003), only about 7% were resolved at 160 μm (Dole et al. 2004). Dole et al. (2006) managed to resolve most of the 70 μm and 160 μm by stacking 24 μm sources.

The cold mission of Spitzer is over, and lots of data are now public. We present extragalactic number counts built homogeneously by combining deep and wide fields. The large sky surface used significantly reduces uncertainties on number counts. In order to obtain very deep FIR number counts, we used a

Table 1. Size, 80% completeness flux density, and calibration scaling factor (see Sect. 2.1) of the used fields.

Field name	Surface area			80% completeness flux			Scaling factor		
	24 μm	70 μm	160 μm	24 μm	70 μm	160 μm	24 μm	70 μm	160 μm
		deg^2		μJy	mJy				
FIDEL eCDFS	0.23	0.19	–	60.	4.6	–	1.0157	1	–
FIDEL EGS	0.41	–	0.38	76.	–	45.	1.0157	–	0.93
COSMOS	2.73	2.41	2.58	96.	7.9	46.	1	0.92	0.96
SWIRE LH	10.04	11.88	11.10	282.	25.4	92.	1.0509	1.10	0.93
SWIRE EN1	9.98	9.98	9.30	261.	24.7	94.	1.0509	1.10	0.93
SWIRE EN2	5.36	5.34	4.98	267.	26.0	90.	1.0509	1.10	0.98
SWIRE ES1	7.45	7.43	6.71	411.	36.4	130.	1.0509	1.10	0.98
SWIRE CDFS	8.42	8.28	7.87	281.	24.7	88.	1.0509	1.10	0.98
SWIRE XMM	8.93	–	–	351.	–	–	1.0509	–	–
Total	53.55	45.51	42.91						

Notes. Some fields are not used at all wavelengths.

stacking analysis and estimate the level of the CIB in the three MIPS bands with them.

2. Data, source extraction and photometry

2.1. Data

We took the public *Spitzer* mosaics[1] from different observation programs: the GOODS/FIDEL (PI: M. Dickinson), COSMOS (PI: D. Sanders) and SWIRE (PI: C. Lonsdale). We used only the central part of each field, which was defined by a cut of 50% of the median coverage for SWIRE fields and 80% for the other. The total area covers 53.6 deg^2, 45.5 deg^2, 42.9 deg^2 at 24 μm, 70 μm and 160 μm respectively. The surface of the deep fields (FIDEL, COSMOS) is about 3.5 deg^2. Some fields were not used at all wavelengths for different reasons: There is no public release of FIDEL CDFS data at 160 μm; the pixels of the EGS 70 μm are not square; XMM is not observed at 70 and 160 μm. Table 1 summarises the field names, sizes and completenesses.

In 2006, new calibration factors were adopted for MIPS (Engelbracht et al. 2007; Gordon et al. 2007; Stansberry et al. 2007). The conversion factor from instrumental unit to MJy/sr is 0.0454 (resp. 702 and 41.7) at 24 μm (resp. 70 μm and 160 μm). The COSMOS GO3 and SWIRE (released 22 Dec. 2006) mosaics were generated with the new calibration. The FIDEL mosaics were obtained with other factors at 24 μm and 160 μm (resp. 0.0447 and 44.7). The 70 μm and 160 μm COSMOS mosaics were color corrected (see Sect. 2.3). Consequently we applied a scaling factor (see Table 1) before the source extraction to each mosaic to work on a homogeneous sample of maps (new calibration and no color correction).

2.2. Source extraction and photometry

The goal is to build homogeneous number counts with well-controlled systematics and high statistics. However, the fields present various sizes and depths. We thus employed a single extraction method at a given wavelength, allowing the heterogeneous datasets to combine in a coherent way.

2.2.1. Mid-IR/far-IR differences

The MIR (24 μm) and FIR (70 μm and 160 μm) maps have different properties: in the MIR, we observe lots of faint blended sources; in the FIR, due to confusion (Dole et al. 2004), all these faint blended sources are only seen as background fluctuations. Consequently, we used different extraction and photometry methods for each wavelength. In the MIR, the priority is the deblending: accordingly we took the SExtractor (Bertin & Arnouts 1996) and PSF fitting. In the FIR, we used efficient methods with strong background fluctuations: wavelet filtering, threshold detection and aperture photometry.

2.2.2. Point spread function (PSF)

The 24 μm empirical PSF of each field is generated with the IRAF (image reduction and analysis facility[2]) DAOPHOT package (Stetson 1987) on the 30 brightest sources of each map. It is normalized in a 12 arcsec radius aperture. Aperture correction (1.19) is computed with the S Tiny Tim[3] (Krist 2006) theoretical PSF for a constant νS_ν spectrum. The difference of correction between a $S_\nu = \nu^{-2}$ and a ν^2 spectrum is less than 2%. So, the hypothesis on the input spectrum is not critical for the PSF normalization.

At 70 μm and 160 μm, we built a single empirical PSF from the SWIRE fields. We used the Starfinder PSF extraction routine (Diolaiti et al. 2000), which median-stacks the brightest non-saturated sources (100 mJy $< S_{70} <$ 10 Jy and 300 mJy $< S_{160} <$ 1 Jy). Previously, fainter neighboring sources were subtracted with a first estimation of the PSF. At 70 μm (resp. 160 μm), the normalization is done in a 35 arcsec (resp. 80 arcsec) aperture, with a sky annulus between 75 arcsec and 125 arcsec (resp. 150 arcsec and 250 arcsec); the aperture correction was 1.21 (resp. 1.20). The theoretical signal in the sky annulus and the aperture correction were computed with the S Tiny Tim Spitzer PSF for a constant νS_ν spectrum. These parameters do not vary more than 5% with the spectrum of sources. Pixels that were affected by the temporal median filtering artifact, which was sometimes present around bright sources, were masked prior to these operations.

2.2.3. Source extraction and photometry

At 24 μm, we detected sources with SExtractor. We chose a Gaussian filter (gauss_5.0_9x9.conv) and a background filter of the size of 64 × 64 pixels. The detection and analysis thresholds were tuned for each field. We performed PSF fitting photometry

[1] from the Spitzer Science Center website: http://data.spitzer.caltech.edu/popular/

[2] http://iraf.noao.edu/

[3] http://ssc.spitzer.caltech.edu/archanaly/contributed/stinytim/

with the DAOPHOT allstar routine. This routine is very efficient for blended sources flux measurement.

At 70 μm and 160 μm, we applied the a-trou wavelet filtering (Starck et al. 1999) on the maps to remove the large scale fluctuations (10 pixels) on which we performed the source detection with a threshold algorithm (Dole et al. 2001, 2004). The threshold was tuned for each field. Photometry was done by aperture photometry on a non filtered map at the positions found on the wavelet filtered map. At 70 μm, we used 10 arcsec aperture radius and a 18 arcsec to 39 arcsec sky annulus. At 160 μm, we used an aperture of 20 arcsec and a 40 arcsec to 75 arcsec annulus. Aperture corrections were computed with the normalized empirical PSF: 3.22 at 70 μm and 3.60 at 160 μm. In order to estimate the uncertainty on this correction, aperture corrections were computed using five PSF built on five different SWIRE fields. The uncertainty is 1.5% at 70 μm and 4.5% at 160 μm.

2.3. Color correction

The MIPS calibration factors were calculated for a 10 000 K blackbody (MIPS Data Handbook 2007[4]). However, the galaxies SED are different and the MIPS photometric bands are large ($\lambda/\Delta\lambda \approx 3$). Thus, color corrections were needed. We used (like Shupe et al. (2008) and Frayer et al. (2009)) a constant νS_ν spectrum at 24 μm, 70 μm and 160 μm. Consequently, all fluxes were divided by 0.961, 0.918 and 0.959 at 24 μm, 70 μm and 160 μm due to this color correction. Another possible convention is $\nu S_\nu \propto \nu^{-1}$. This convention is more relevant for the local sources at 160 μm, whose spectrum decreases quickly with wavelength. Nevertheless, the redshifted sources studied by stacking are seen at their peak of the cold dust emission, and their SED agrees better with the constant νS_ν convention. The difference of color correction between these two conventions is less than 2%, and this choice is thus not critical. We consequently chose the constant νS_ν convention to more easily compare our results with Shupe et al. (2008) and Frayer et al. (2009).

3. Catalog properties

3.1. Spurious sources

Our statistical analysis may suffer from spurious sources. We have to estimate how many false detections are present in a map and what their flux distribution is. To do so, we built a catalog with the flipped map. To build this flipped map, we multiplied the values of the pixels of the original map by a factor of –1. Detection and photometry parameters were exactly the same as for normal catalogs. At 24 μm, there are few spurious sources (<10%) in bins brighter than the 80% completeness limit flux density. At 70 μm and 160 μm, fluctuations of the background due to unresolved faint sources are responsible for spurious detections. Nevertheless, the ratio between detected source numbers and fake source numbers stayed reasonable (below 0.2) down to the 80% completeness limit (see the example of FIDEL CDFS at 70 μm in Fig. 1).

3.2. Completeness

The completeness is the probability to extract a source of a given flux. To estimate it, we added artificial sources (based on empirical PSF) on the initial map and looked for a detection in a 2 arcsec radius at 24 μm around the initial position (8 arcsec at 70 μm and 16 arcsec at 160 μm). This operation was done for different fluxes with a Monte-Carlo simulation. We chose the number of artificial sources in each realization in a way that they have less than 1% probability to fall at a distance shorter than 2 PSF FWHM (full width at half maximum). The completeness is plotted in Fig. 2, and the 80% completeness level is reported in Table 1.

[4] http://ssc.spitzer.caltech.edu/mips/dh/

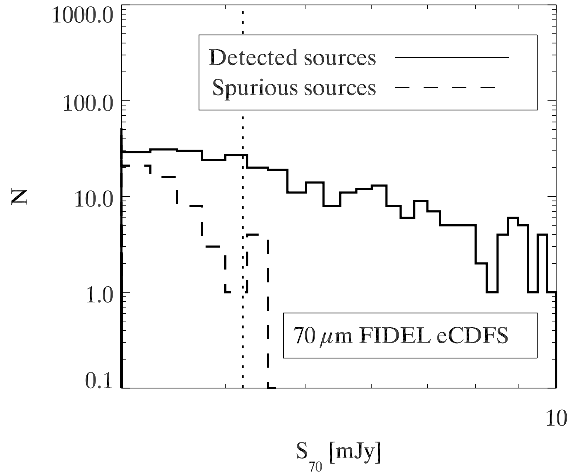

Fig. 1. Flux distribution of sources extracted from normal *(solid line)* and flipped *(dash line)* maps, at 70 μm in FIDEL eCDFS. The vertical dashed line represents the 80% completeness flux density.

3.3. Photometric accuracy

The photometric accuracy was checked with the same Monte-Carlo simulation. For different input fluxes, we built histograms of measured fluxes and computed the median and scatter of these distributions. At lower fluxes, fluxes are overestimated and errors are larger. These informations were used to estimate the Eddington bias (see next section). The photometric accuracy at 70 μm in FIDEL CDFS is plotted as an example in Fig. 3.

We also compared our catalogs with published catalogs. At 24 μm, we compared it with the GOODS CDFS catalog of Chary et al. (2004), and the COSMOS catalog of LeFloc'h et al. (2009). Their fluxes were multiplied by a corrective factor to be compatible with the νS_ν = constant convention. Sources were considered to be the same if they are separated by less than 2 arcsec. We computed the standard deviation of the distribution of the ratio between our and their catalogs. In a 80–120 μJy bin in the CDFS, we found a dispersion of 19%. In a 150–250 μJy bin in COSMOS, we found a scatter of 13%. The offset is +3% with COSMOS catalog and –1% with GOODS catalog. At 70 and 160 μm, we compared our catalogs with the COSMOS and SWIRE team ones. In all cases, the scatter is less than 15%, and the offset is less than 3%. At all wavelengths and for all fields, the offset is less than the calibration uncertainty.

3.4. Eddington bias

When sources become fainter, photometric errors increase. In addition, fainter sources are more numerous than brighter ones (in general $dN/dS \sim S^{-r}$). Consequently, the number of sources in faint bins are overestimated. This is the classical Eddington

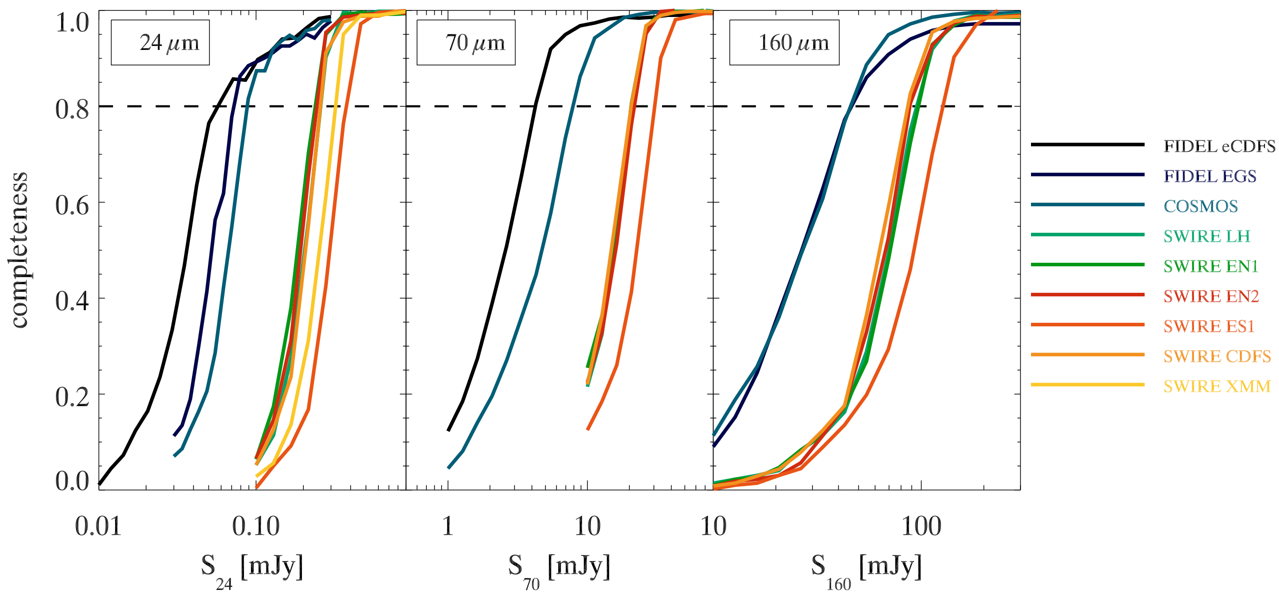

Fig. 2. Completeness at 24 μm *(left)*, 70 μm (*center*), and 160 μm (*right*) as a function of the source flux for all fields. The dashed line represents 80% completeness.

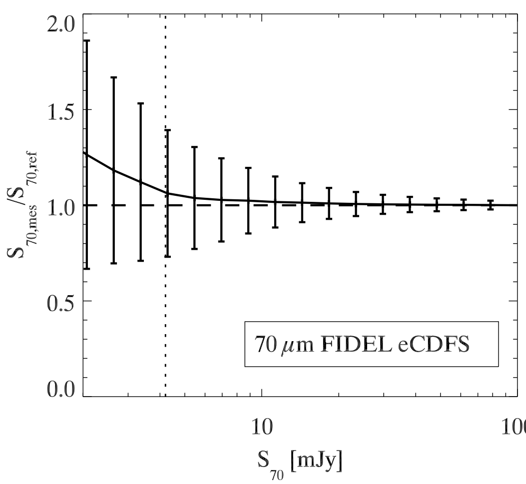

Fig. 3. Ratio between measured flux and input flux computed from Monte Carlo simulations at 70 μm in FIDEL eCDFS. Error bars represent 1σ dispersion. The vertical dashed line represents the 80% completeness flux density.

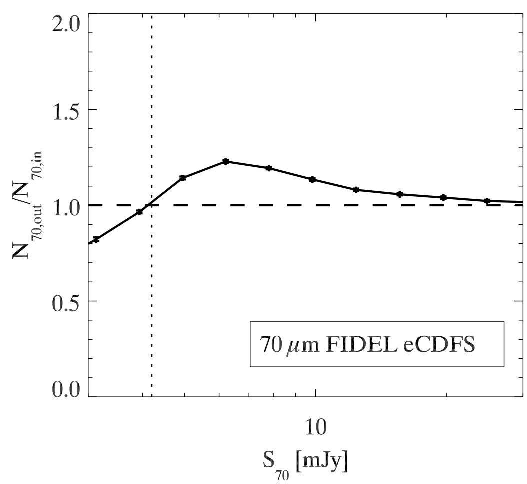

Fig. 4. Eddington bias: ratio between the number of detected sources and the number of input sources at 70 μm in FIDEL eCDFS. The vertical dashed line represents the 80% completeness flux density.

bias (Eddington 1913, 1940). The example of FIDEL CDFS at 70 μm is plotted in Fig. 4.

To correct for this effect at 70 μm and 160 μm, we estimated a correction factor for each flux bin. We generated an input flux catalog with a power-law distribution (r = 1.6 at 70 μm, r = 3 at 160 μm). We took into account completeness and photometric errors (coming from Monte-Carlo simulations) to generate a mock catalog. We then computed the ratio between the number of mock sources found in a bin and the number of input sources. This task was done for all fields. This correction is more important for large r (at 160 μm). At 24 μm, thanks to the PSF fitting, the photometric error is more reduced and symmetrical. Less faint sources are thus placed in brighter flux bins. Because of this property and the low r (about 1.45), this correction can be ignored for 24 μm counts.

4. Number counts

4.1. Removing stars from the catalogs

To compute extragalactic number counts at 24 μm, we removed the stars with the $K - [24] < 2$ color criterion and identification procedure following Shupe et al. (2008). The K band magnitudes were taken from the 2MASS catalog (Skrutskie et al. 2006). We ignored the star contribution at 70 μm and 160 μm, which is negligible (<1% in all used flux density bins) according to the DIRBE Faint Count model (Arendt et al. 1998).

4.2. 24 μm number counts

We counted the number of extragalactic sources for each field and in each flux bin. We subtracted the number of spurious detections (performed on the flipped map). We divided by the

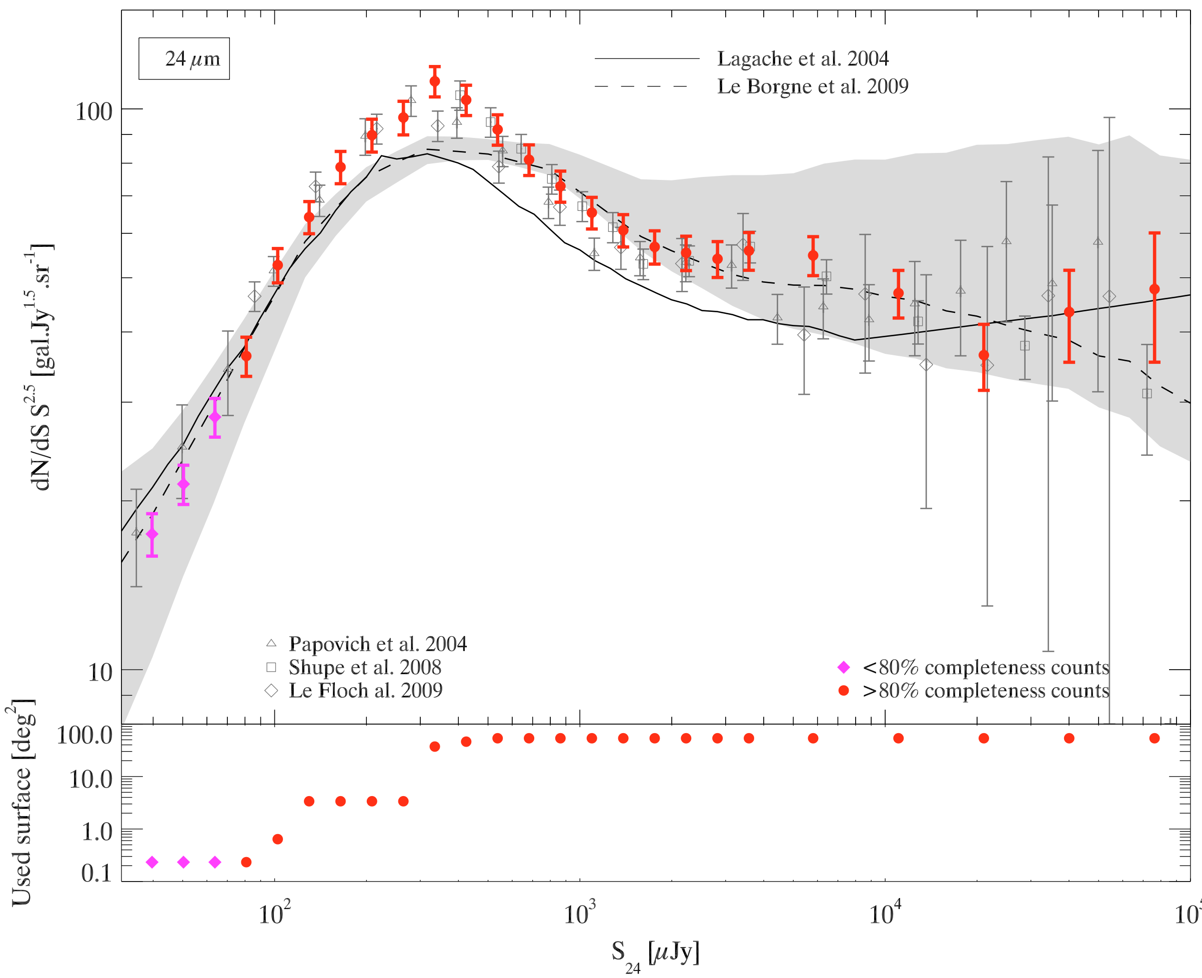

Fig. 5. Differential number counts at 24 μm. *Filled circle*: points obtained with ≥80% completeness; *filled diamond*: points obtained with a 50% to 80% completeness; *open triangle*: Papovich et al. (2004) GTO number counts obtained with PSF fitting photometry; *open square*: Shupe et al. (2008) SWIRE number counts obtained with aperture photometry; *open diamond*: LeFloc'h et al. (2009) COSMOS number counts obtained with PSF fitting photometry; *continuous line*: Lagache et al. (2004) model; *dashed line and grey region*: Le Borgne et al. (2009) model and 90% confidence region. Error bars take into accounts clustering (see Sect. 4.5) and calibration uncertainties (Engelbracht et al. 2007).

completeness. As a next step, the counts of all fields were combined together with a mean weighted by field size. Actually, a weighting by the number of sources in each field overweighs the denser fields and biases the counts. Counts from a field were combined only if the lower end of the flux bin was larger then or equal to the 80% completeness. We thus reached 71 μJy (71 μJy to 90 μJy bin) in the counts. However, to probe fainter flux densities, we used the data from the deepest field (FIDEL eCDFS) between a 50 and 80% completeness, allowing us to reach 35 μJy.

Our number counts are plotted in Fig. 5 and are written in Table 2. We also plot data from Papovich et al. (2004), Shupe et al. (2008) and LeFloc'h et al. (2009), and model predictions from Lagache et al. (2004) and Le Borgne et al. (2009). The Papovich et al. (2004) fluxes are multiplied by a factor 1.052 to take into account the update in the calibration, the color correction and the PSF. This correction of flux also implies a correction on number counts, according to:

$$\left(\frac{dN}{dS_f}S_f^{2.5}\right)_{S_f} = \left(c^{1.5}\frac{dN}{dS_i}S_i^{2.5}\right)_{cS_i}, \quad (1)$$

where S_i is the initial flux, S_f is the corrected flux and c the corrective factor ($S_f = cS_i$). A correction of the flux thus corresponds to a shift in the abscissa (factor c) and in the ordinate (factor $c^{1.5}$). Papovich et al. (2004) do not subtract stars and thus overestimate counts above 10 mJy. We have a very good agreement with their work below 10 mJy. We also have a very good agreement with Shupe et al. (2008). The LeFloc'h et al. (2009) fluxes are multiplied by 1.05 to take into account a difference of the reference SED: 10 000 K versus constant νS_ν, and by another correction of 3% corresponding to the offset observed in Sect. 3.3. There is an excellent agreement with their work.

The Lagache et al. (2004)[5] and Le Borgne et al. (2009)[6] generally agree well with the data, in particular on the faint end below 100 μJy, and on the position of the peak around 300 μJy. However, the Lagache et al. (2004) model slightly underestimates (about 10%) the counts above 200 μJy. The Le Borgne et al. (2009) model is flatter than the data, and agrees reasonably well above 600 μJy.

[5] Lagache et al. (2004) model used a ΛCDM cosmology with $\Omega_\Lambda = 0.73$, $\Omega_M = 0.27$ and $h = 0.71$.

[6] Le Borgne et al. (2009) model used a ΛCDM cosmology with $\Omega_\Lambda = 0.7$, $\Omega_M = 0.3$ and $h = 0.7$.

Table 2. Differential number counts at 24 μm.

$\langle S \rangle$	S_{min}	S_{max}	$dN/dS.S^{2.5}$	$\sigma_{poisson}$	$\sigma_{clustering}$	$\sigma_{clus.+calib.}$	Ω_{used}
	(in mJy)			(in gal $Jy^{1.5}$ sr^{-1})			deg^2
0.040	0.035	0.044	17.5	1.0	1.1	1.3	0.2
0.050	0.044	0.056	21.4	1.0	1.1	1.4	0.2
0.064	0.056	0.071	28.2	1.2	1.5	1.8	0.2
0.081	0.071	0.090	36.2	1.5	1.9	2.4	0.2
0.102	0.090	0.114	52.6	1.3	1.9	2.9	0.6
0.130	0.114	0.145	64.1	1.0	1.7	3.1	3.4
0.164	0.145	0.184	78.7	1.1	2.2	3.8	3.4
0.208	0.184	0.233	89.8	1.3	2.8	4.5	3.4
0.264	0.233	0.295	96.5	1.5	3.3	5.1	3.4
0.335	0.295	0.374	112.0	0.8	1.8	4.8	37.2
0.424	0.374	0.474	103.7	0.6	1.7	4.5	46.1
0.538	0.474	0.601	91.9	0.6	1.5	4.0	53.6
0.681	0.601	0.762	81.2	0.6	1.5	3.6	53.6
0.863	0.762	0.965	72.8	0.7	1.6	3.3	53.6
1.094	0.965	1.223	65.3	0.8	1.6	3.1	53.6
1.387	1.223	1.550	60.8	0.9	1.7	3.0	53.6
1.758	1.550	1.965	56.7	1.0	1.8	2.9	53.6
2.228	1.965	2.490	55.4	1.2	2.1	3.0	53.6
2.823	2.490	3.156	54.0	1.5	2.3	3.2	53.6
3.578	3.156	4.000	55.9	1.8	2.7	3.5	53.6
5.807	4.000	7.615	54.8	1.5	2.9	3.6	53.6
11.055	7.615	14.496	46.9	2.3	3.6	4.1	53.6
21.045	14.496	27.595	36.4	3.3	4.4	4.6	53.6
40.063	27.595	52.531	43.4	5.9	7.7	7.9	53.6
76.265	52.531	100.000	47.7	9.9	12.0	12.2	53.6

Notes. $\sigma_{clustering}$ is the uncertainty taking into account clustering (see Sect. 4.5). $\sigma_{clus.+calib.}$ takes into account both clustering and calibration (Engelbracht et al. 2007).

Table 3. Differential number counts at 70 μm.

$\langle S \rangle$	S_{min}	S_{max}	$dN/dS.S^{2.5}$	$\sigma_{poisson}$	$\sigma_{clustering}$	$\sigma_{clus.+calib.}$	Ω_{used}
	(in mJy)			(in gal $Jy^{1.5}$ sr^{-1})			deg^2
4.197	3.500	4.894	2073.	264.	309.	342.	0.2
5.868	4.894	6.843	2015.	249.	298.	330.	0.2
8.206	6.843	9.569	1690.	289.	332.	353.	0.2
11.474	9.569	13.380	2105.	123.	202.	250.	2.6
16.044	13.380	18.708	2351.	148.	228.	281.	2.6
22.434	18.708	26.159	1706.	153.	208.	240.	2.6
31.369	26.159	36.578	2557.	69.	124.	218.	38.1
43.862	36.578	51.146	2446.	73.	123.	211.	45.5
61.331	51.146	71.517	2359.	90.	141.	217.	45.5
85.758	71.517	100.000	2257.	112.	164.	228.	45.5
157.720	100.000	215.440	2354.	121.	198.	257.	45.5
339.800	215.440	464.160	2048.	200.	276.	311.	45.5
732.080	464.160	1000.000	2349.	381.	500.	526.	45.5

Notes. $\sigma_{clustering}$ is the uncertainty taking into account clustering (see Sect. 4.5). $\sigma_{clus.+calib.}$ takes into account both clustering and calibration (Gordon et al. 2007).

4.3. 70 μm number counts

Counts in the flux density bins brighter than the 80% completeness limit were obtained in the same way as at 24 μm (Fig. 6 and Table 3). In addition, they were corrected from the Eddington bias (cf. Sect. 3.4). We reached about 4.9 mJy at 80% completeness (4.9 to 6.8 bin). We used CDFS below 80% completeness limit to probe fainter flux density level. We cut these counts at 3.5 mJy. At this flux density, the spurious rate reached 50%. We used a stacking analysis to probe fainter flux density levels (cf. Sect. 5).

We can see breaks in the counts around 10 mJy and 20 mJy. These breaks appear between points built with a different set of fields. Our counts agree with earlier works of Dole et al. (2004), Frayer et al. (2006) and Frayer et al. (2009). However, these works suppose only a Poissonian uncertainty, which underestimates the error bars (see Sect. 4.5). Our data also agree well with these works. The Lagache et al. (2004) model agrees well with our data. The Le Borgne et al. (2009) model gives a reasonable fit, despite an excess of about 30% between 3 mJy and 10 mJy.

Table 4. Differential number counts at 160 μm. $\sigma_{clustering}$ is the uncertainty taking into account clustering (see Sect. 4.5).

$\langle S \rangle$	$S_{\rm min}$	$S_{\rm max}$	$dN/dS.S^{2.5}$	$\sigma_{\rm poisson}$	$\sigma_{\rm clustering}$	$\sigma_{\rm clus.+calib.}$	$\Omega_{\rm used}$
	(in mJy)			(in gal $Jy^{1.5}$ sr^{-1})			deg^2
45.747	40.000	51.493	16855.	1312.	2879.	3519.	3.0
58.891	51.493	66.289	14926.	1243.	2704.	3243.	3.0
75.813	66.289	85.336	13498.	1319.	2648.	3104.	3.0
97.596	85.336	109.860	12000.	1407.	2442.	2835.	3.0
125.640	109.860	141.420	10687.	457.	991.	1621.	36.2
161.740	141.420	182.060	7769.	425.	773.	1211.	42.9
208.210	182.060	234.370	7197.	472.	810.	1184.	42.9
268.040	234.370	301.710	5406.	487.	734.	979.	42.9
345.050	301.710	388.400	5397.	585.	843.	1063.	42.9
444.200	388.400	500.000	4759.	662.	891.	1059.	42.9
750.000	500.000	1000.000	6258.	685.	1158.	1380.	42.9
1500.000	1000.000	2000.000	4632.	989.	1379.	1487.	42.9

Notes. $\sigma_{clus.+calib.}$ takes into account both clustering and calibration (Stansberry et al. 2007).

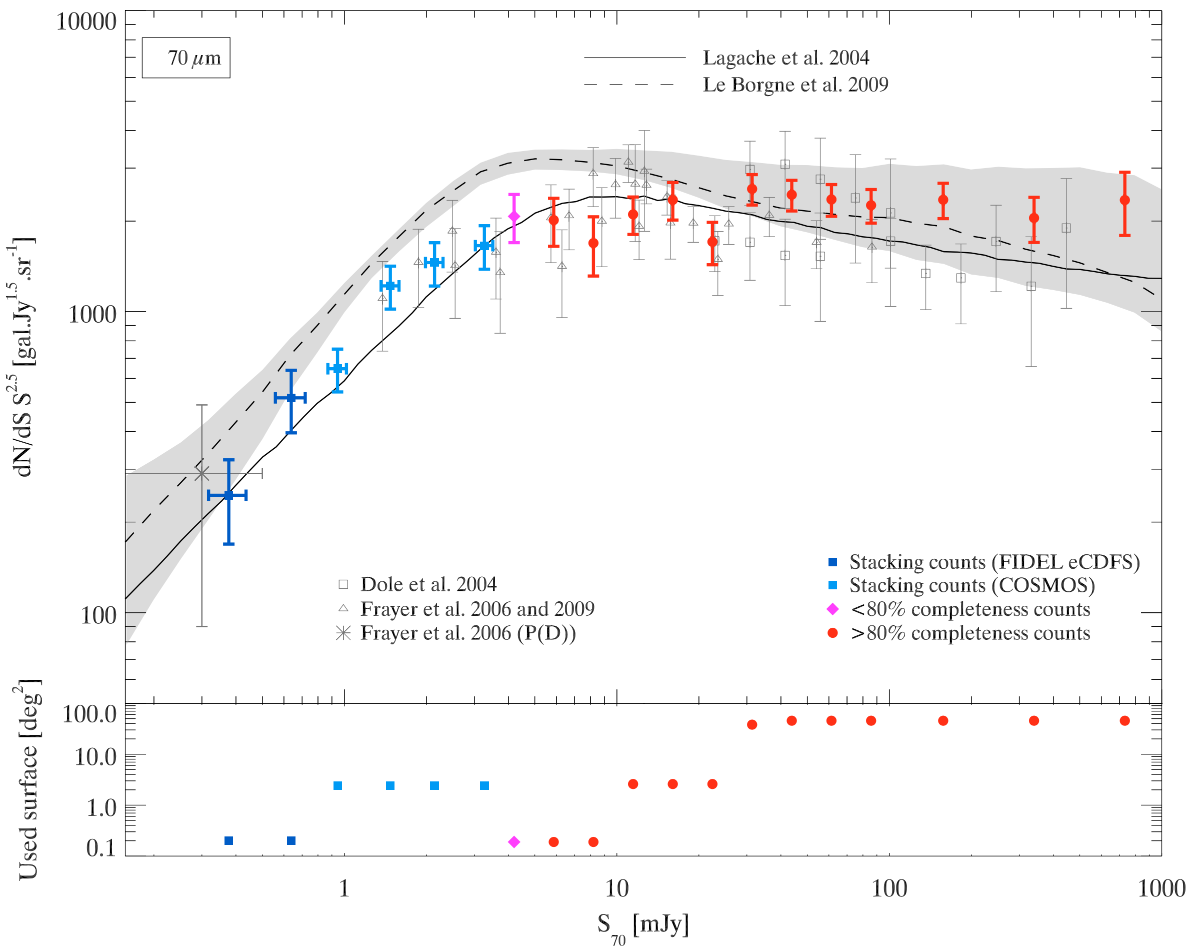

Fig. 6. Differential number counts at 70 μm. *Filled circle*: points obtained with ≥80% completeness; *filled diamond*: points obtained with less than 50% spurious sources and less than 80% completeness; *filled square*: stacking number counts (clear: FIDEL eCDFS, dark: COSMOS); *open square*: Dole et al. (2004) number counts in CDFS, Bootes and Marano; *open triangle*: Frayer et al. (2006) in GOODS and Frayer et al. (2009) in COSMOS; *cross*: Frayer et al. (2006) deduced from background fluctuations; *continuous line*: Lagache et al. (2004) model; *dashed line and grey region*: Le Borgne et al. (2009) model and 90% confidence region. Error bars take into account clustering (see Sect. 4.5) and calibration uncertainties (Gordon et al. 2007).

4.4. 160 μm number counts

The 160 μm number counts were obtained exactly in the same way as at 70 μm. We used COSMOS and EGS to probe counts below the 80% completeness limit. We reached 51 mJy at 80% completeness (51 mJy to 66 mJy bin) and 40 mJy for the 50% spurious rate cut (Fig. 7 and Table 4). We used a stacking analysis to probe fainter flux density levels (cf. Sect. 5).

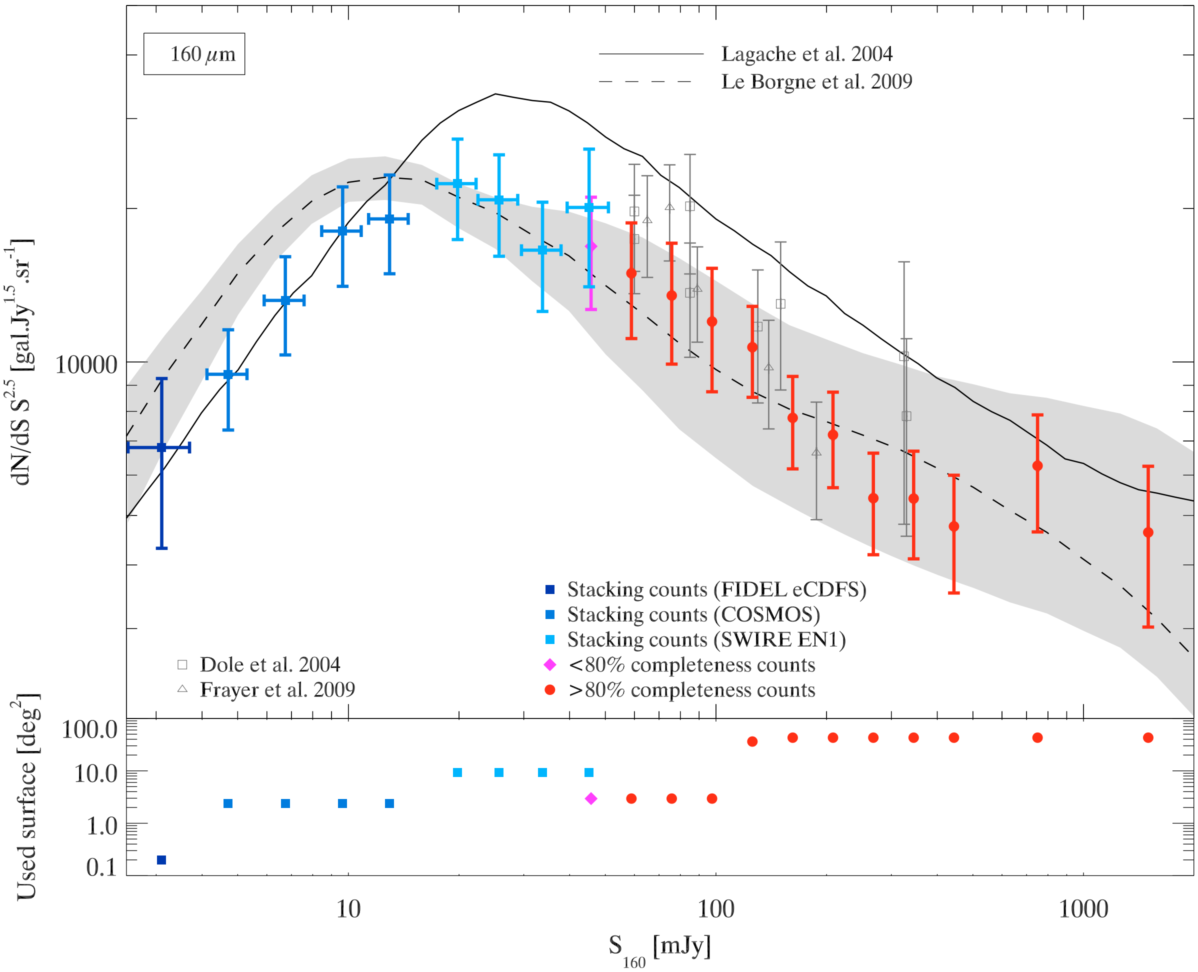

Fig. 7. Differential number counts at 160 μm. *Filled circle*: points obtained with ≥80% completeness; *filled diamond*: points obtained with less than 50% spurious sources and less than 80% completeness; *filled square*: stacking number counts (clear: FIDEL/GTO CDFS, *middle*: COSMOS, dark: SWIRE EN1); *open square*: Dole et al. (2004) number counts in CDFS and Marano; *open triangle*: Frayer et al. (2009) in COSMOS; *continuous line*: Lagache et al. (2004) model; *dashed line and grey region*: Le Borgne et al. (2009) model and 90% confidence region. Error bars take into account clustering (see Sect. 4.5) and calibration uncertainties (Stansberry et al. 2007).

Our counts agree with the earlier works of Dole et al. (2004) and Frayer et al. (2009). We find like Frayer et al. (2009) that the Lagache et al. (2004) model overestimates the counts by about 30% above 50 mJy (see the discussion in Sect. 7.2). On the contrary, the Le Borgne et al. (2009) model underpredicts the counts by about 20% between 50 mJy and 150 mJy.

4.5. Uncertainties on number counts including clustering

Shupe et al. (2008) showed that the SWIRE field-to-field variance is significantly higher than the Poisson noise (by a factor of three in some flux bins). They estimated their uncertainties on number counts with a field bootstrap method. We used a more formal method to deal with this problem.

The uncertainties on the number counts are Poissonian only if sources are distributed uniformly. But, actually, the infrared galaxies are clustered. The uncertainties must thus be computed taking into account clustering. We first measured the source clustering as a function of the flux density with the counts-in-cells moments (c-in-c) method (Peebles 1980; Szapudi 1998; Blake & Wall 2002). We then computed the uncertainties knowing these clustering properties of the sources, the source density in the flux density bins and the field shapes. The details are explained in the Appendix A.

This statistical uncertainty can be combined with the *Spitzer* calibration uncertainty (Engelbracht et al. 2007; Gordon et al. 2007; Stansberry et al. 2007) to compute the total uncertainty on differential number counts.

5. Deeper FIR number counts using a stacking analysis

5.1. Method

The number counts derived in Sect. 4 show that down to the 80% completeness limit, the source surface density is 24100 deg^{-2}, 1200 deg^{-2}, and 220 deg^{-2} at 24, 70, and 160 μm, respectively, i.e. 20 times (resp. 110 times) higher at 24 μm than at 70 μm (resp. 160 μm). These differences can be explained by the angular resolution decreasing with increasing wavelength, thus increasing confusion, and the noise properties of the detectors. There are thus many 24 μm sources without detected FIR counterparts. If we want to probe deeper into the FIR number counts, we can take advantage of the information provided by the 24 μm data, namely the existence of infrared galaxies not necessarily detected in the FIR, and their positions.

We used a stacking analysis (Dole et al. 2006) to determine the FIR/MIR color as a function of the MIR flux. With this information, we can convert MIR counts into FIR counts. The stacking technique consists in piling up very faint far-infrared galaxies which are not detected individually, but are detected at 24 μm. For this purpose, it makes use of the 24 μm data prior to tracking their undetected counterpart at 70 μm and 160 μm, where most of the bolometric luminosity arises. This method was used by Dole et al. (2006), who managed to resolve the FIR CIB using 24 μm sources positions, as well many other authors (e.g Serjeant et al. (2004); Dye et al. (2006); Wang et al. (2006); Devlin et al. (2009); Dye et al. (2009); Marsden et al. (2009); Pascale et al. (2009)).

To derive the 70 μm or 160 μm versus 24 μm color, we stacked the FIR maps (cleaned of bright sources) at the positions of the 24 μm sources sorted by flux, and performed aperture photometry (same parameters as in Sect. 2). We thus get

$$\overline{S_{\rm FIR}} = f(\overline{S_{24}}), \tag{2}$$

where $\overline{S_{\rm FIR}}$ is the average flux density in the FIR of the population selected at 24 μm, $\overline{S_{24}}$ the average flux density at 24 microns, and f is the function linking both quantities. We derive f empirically using the $S_{\rm FIR}$ versus S_{24} relation obtained from stacking.

We checked that f is a smooth monotonic function, in agreement with the expectation that the color varies smoothly with the redshift and the galaxy emission properties. Assuming that the individual sources follow this relation exactly, the FIR number counts could be deduced from

$$\left.\frac{dN}{dS_{\rm FIR}}\right|_{S_{\rm FIR}=f(S_{24})} = \left.\frac{dN}{dS_{24}}\right|_{S_{24}} \Big/ \left.\frac{dS_{\rm FIR}}{dS_{24}}\right|_{S_{24}}. \tag{3}$$

In practice, the two first terms are discrete. In addition, the last term is computed numerically in the same S_{24} bin, using the two neighboring flux density bins ($k-1$ and $k+1$). We finally get

$$\frac{dN}{dS_{\rm FIR}}(\overline{S_{{\rm FIR}\,k}}) = \left(\frac{dN}{dS_{24}}\right)_k \Big/ \frac{\overline{S_{{\rm FIR},k+1}} - \overline{S_{{\rm FIR},k-1}}}{\overline{S_{24,k+1}} - \overline{S_{24,k-1}}}, \tag{4}$$

where $\langle S_{\rm FIR}\rangle$ is measured by stacking. In reality, sources do not follow Eq. (2) exactly, but exhibit a scatter around this mean relation

$$S_{\rm FIR} = f(S_{24}) + \sigma. \tag{5}$$

Our method is still valid under the condition $\frac{\sigma}{f} \ll 1$, and we verify its validity with simulations (see next section).

To obtain a better signal to noise ratio, we cleaned the resolved bright sources from the FIR maps prior to stacking. We used 8 S_{24} bins per decade. We stacked a source only if the coverage was more than half of the median coverage of the map. Uncertainties on the FIR mean flux were estimated with a bootstrap method. Furthermore, knowing the uncertainties on the 24 μm number counts and the mean S_{24} fluxes, we deduced the uncertainties on the FIR number counts according to Eq. (4).

At 70 μm, we used the FIDEL eCDFS (cleaned at S_{70} > 10 mJy) and the COSMOS (cleaned at S_{70} > 50 mJy) fields. At 160 μm, we used 160 μm the GTO CDFS (cleaned at S_{160} > 60 mJy), the COSMOS (cleaned at S_{160} > 100 mJy) and the SWIRE EN1 (no clean to probe the S_{160} > 20 mJy sources) fields.

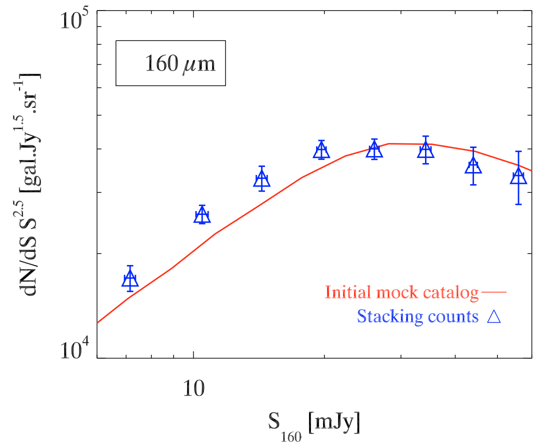

Fig. 8. Simulated number counts at 160 μm, computed from stacking counts *(triangle)* and from the input mock catalog *(solid line)*. The good agreement (better than 15%) validates the stacking counts method (see Sect. 5.2). Twenty realizations of the 2.9 deg^2 field maps with about 870 000 mock sources each were used.

5.2. Validation on simulations

We used the Fernandez-Conde et al. (2008) simulations[7] to validate our method. These simulations are based on the Lagache et al. (2004) model, and include galaxy clustering. We employed 20 simulated mock catalogs of a 2.9 deg^2 field each, containing about 870 000 mock sources each. The simulated maps have the same pixel size as the actual Spitzer mosaics (1.2″, 4″, and 8″ at 24 μm, 70 μm, and 160 μm, resp.) and are convolved with our empirical PSF. A constant standard deviation Gaussian noise was added. We applied the same method as for the real data to produce stacking number counts. At 160 μm, for bins below 15 mJy, we cleaned the sources brighter than 50 mJy. Figure 8 shows 160 μm number counts from the mock catalogs down to S_{160} = 1 mJy (diamond) and the number counts deduced from the stacking analysis described in the previous section (triangle). The error bars on the figure are the standard deviations of the 20 realization. There is a good agreement between the stacking counts and the classical counts (better than 15%). Nevertheless, we observed a systematic bias, intrinsic to the method, of about 10% in some flux density bins. We thus combined this 10% error with the statistical uncertainties to compute our error bars. We also validated the estimation of the statistical uncertainty in the stacking counts: we check that the dispersion of the counts obtained by stacking, coming from different realizations, was compatible with our estimation of statistical uncertainties. The results are the same at 70 μm.

5.3. Results

At 70 μm, the stacking number counts reach 0.38 mJy (see Fig. 6 and Table 5). The last stacking point is compatible with the Frayer et al. (2006) P(D) constraint. The stacking points also agree very well with the Lagache et al. (2004) model. The Le Borgne et al. (2009) model predicts slightly too many sources in 0.3 to 3 mJy range. The turnover around 3 mJy and the power law behavior of the faint counts (S_{70} < 2 mJy), observed by Frayer et al. (2006) are confirmed with a better accuracy.

At 160 μm, the stacking counts reach 3.1 mJy (see Fig. 7 and Table 6). We observed for the first time a turnover at about

[7] Publicly available at http://www.ias.u-psud.fr/irgalaxies/

Table 5. Stacking extragalactic number counts at 70 μm.

$\langle S \rangle$ (in mJy)	$dN/dS.S^{2.5}$ (in gal $Jy^{1.5}$ sr^{-1})	$\sigma_{clus.}$	$\sigma_{clus.+calib.}$	Field
0.38 ± 0.05	246.	72.	76.	FIDEL CDFS
0.64 ± 0.07	517.	109.	122.	FIDEL CDFS
0.94 ± 0.03	646.	80.	105.	COSMOS
1.48 ± 0.04	1218.	151.	198.	COSMOS
2.14 ± 0.05	1456.	183.	239.	COSMOS
3.27 ± 0.07	1657.	211.	273.	COSMOS

Notes. $\sigma_{clus.}$ is the uncertainty taking into account clustering (see Sect. 4.5). $\sigma_{clus.+calib.}$ takes into account both clustering and calibration (Gordon et al. 2007).

Table 6. Stacking extragalactic number counts at 160 μm.

$\langle S \rangle$ (in mJy)	$dN/dS.S^{2.5}$ (in gal $Jy^{1.5}$ sr^{-1})	$\sigma_{clus.}$	$\sigma_{clus.+calib.}$	Field
3.11 ± 0.46	6795.	2163.	2485.	GTO CDFS
4.71 ± 0.16	9458.	1236.	2104.	COSMOS
6.74 ± 0.22	13203.	1627.	2880.	COSMOS
9.65 ± 0.26	18057.	2307.	3986.	COSMOS
12.95 ± 0.37	19075.	2388.	4182.	COSMOS
19.82 ± 0.48	22366.	2944.	4987.	SWIRE EN1
25.71 ± 0.81	20798.	2811.	4682.	SWIRE EN1
33.74 ± 0.98	16567.	2671.	4004.	SWIRE EN1
45.18 ± 2.08	20089.	4849.	6049.	SWIRE EN1

Notes. $\sigma_{clus.}$ is the uncertainty taking into account clustering (see Sect. 4.5). $\sigma_{clus.+calib.}$ takes into account both clustering and calibration (Stansberry et al. 2007).

20 mJy, and a power-law decrease at smaller flux densities. The stacking counts are lower than the Lagache et al. (2004) model around 20 mJy (about 30%). Below 15 mJy, the stacking counts agree with this model. The Le Borgne et al. (2009) model agree quite well with our points below 20 mJy. The results at 160 μm will be discussed in Sect. 7.2.

6. New lower limits and estimates of the CIB at 24 μm, 70 μm and 160 μm

6.1. 24 μm CIB: lower limit and estimate

By integrating the measured 24 μm number counts between 35 μJy and 0.1 Jy, we can estimate a lower value of the CIB at this wavelength. The counts were integrated with a trapeze method. We estimated the uncertainty on the integral by adding (on 10000 realisations) a random Gaussian error to each data point with the σ given by the count uncertainties taking into account clustering. We then added the 4% calibration error of the instrument (Engelbracht et al. 2007). We found $2.26^{+0.09}_{-0.09}$ nW m^{-2} sr^{-1}. The very bright source counts (S_{24} > 0.1 Jy) are supposed to be euclidian ($dN/dS = C_{eucl} S^{2.5}$). We used the three brightest points to estimate C_{eucl}. We found a contribution to the CIB of $0.032^{+0.003}_{-0.003}$ nW m^{-2} sr^{-1}. Consequently, very bright sources extrapolation is not critical for the CIB estimation (1% of CIB). The contribution of $S_{24} > 35$ μJy is thus $2.29^{+0.09}_{-0.09}$ nW m^{-2} sr^{-1} (cf. Table 7).

We might have wanted to estimate the CIB value at 24 μm. To do so, we needed to extrapolate the number counts on the faint end. Below 100 μJy, the number counts exhibit a power-law behavior (Fig. 5). We assumed that this behavior (of the form $dN/dS = C_{faint} S^r$) still holds below 35 μJy. r and C_{faint} are determined using the four faintest bins. We found $r = 1.45 \pm 0.10$ (compatible with 1.5 ± 0.1 of Papovich et al. 2004). Our new estimate of the CIB at 24 μm due to infrared galaxies is thus $2.86^{+0.19}_{-0.16}$ nW m^{-2} sr^{-1}. The results are plotted in Fig. 9. We conclude that resolved sources down to S_{24} = 35 μJy account for 80% of the CIB at this wavelength.

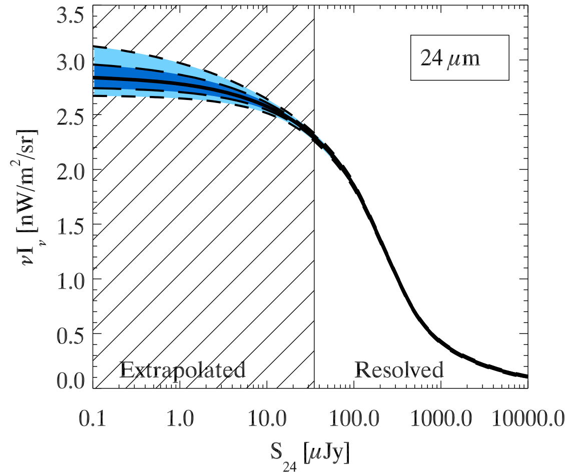

Fig. 9. Cumulative contribution to the surface brightness of the 24 μm CIB as a function of $S_{24\,\mu m}$. The colored area represents the 68% and 95% confidence level. The shaded area represents the $S_{24} < 35\mu$Jy power-law extrapolation zone (see Sect. 6.1). The 4% calibration uncertainty is not represented. The table corresponding to this figure is available online at http://www.ias.u-psud.fr/irgalaxies/

Table 7. Summary of CIB results found in this article.

		24 μm	70 μm	160 μm
$S_{cut,resolved}$	mJy	0.035	3.50	40.0
$S_{cut,stacking}$		–	0.38	3.1
$\nu B_{\nu,resolved}$	nW m^{-2} sr^{-1}	$2.29^{+0.09}_{-0.09}$	$3.1^{+0.2}_{-0.2}$	$1.0^{+0.1}_{-0.1}$
$\nu B_{\nu,resolved+stacking}$		–	$5.4^{+0.4}_{-0.4}$	$8.9^{+1.1}_{-1.1}$
$\nu B_{\nu,tot}$		$2.86^{+0.19}_{-0.16}$	$6.6^{+0.7}_{-0.6}$	$14.6^{+7.1}_{-2.9}$

6.2. 70 μm and 160 μm CIB: lower limit and estimate

At 70 μm and 160 μm, the integration of the number counts was done in the same way as at 24 μm, except for the stacking counts, which are correlated. To compute the uncertainties on the integral, we added (on 10 000 realizations) a Gaussian error simultaneously to the three quantities and completely recomputed the associated stacking counts: 1- the mean density flux given by the stacking; 2- the 24 μm number counts; 3- the mean 24 μm flux density. At 70 μm, and 160 μm, the calibration uncertainty is 7% (Gordon et al. 2007) and 12% (Stansberry et al. 2007), respectively. We estimated the CIB surface brightness contribution of resolved sources (S_{70} > 3.5 mJy and S_{160} > 40 mJy) of $3.1^{+0.2}_{-0.2}$ nW m^{-2} sr^{-1} and $1.0^{+0.1}_{-0.1}$ nW m^{-2} sr^{-1}. The contribution of S_{70} > 0.38 mJy and S_{160} > 3.1 mJy is $5.4^{+0.4}_{-0.4}$ nW m^{-2} sr^{-1} and $8.9^{+1.1}_{-1.1}$ nW m^{-2} sr^{-1}, respectively.

Below 2 mJy at 70 μm, and 10 mJy at 160 μm, the stacking counts are compatible with a power-law. Like at 24 μm, we assumed that this behavior can be extrapolated and determined the law with the five faintest bins at 70 μm, and the four faintest at 160 μm. We found a slope r = 1.50 ± 0.14 at 70 μm, and

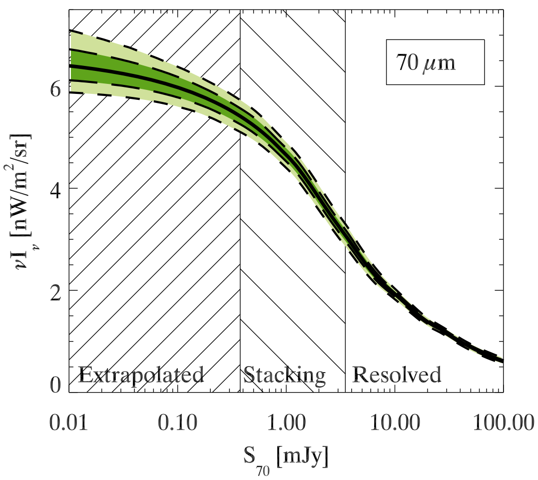

Fig. 10. Cumulative contribution to the surface brightness of the 70 μm CIB as a function of $S_{70\,\mu m}$. The colored area represents the 68% and 95% confidence level. The shaded areas represent the $0.38 < S_{70} < 3.3$ mJy stacking counts zone and the $S_{70} < 0.38$ mJy power-law extrapolation zone (see Sect. 6.2). The 7% calibration uncertainty is not represented. The table corresponding to this figure is available online at http://www.ias.u-psud.fr/irgalaxies/

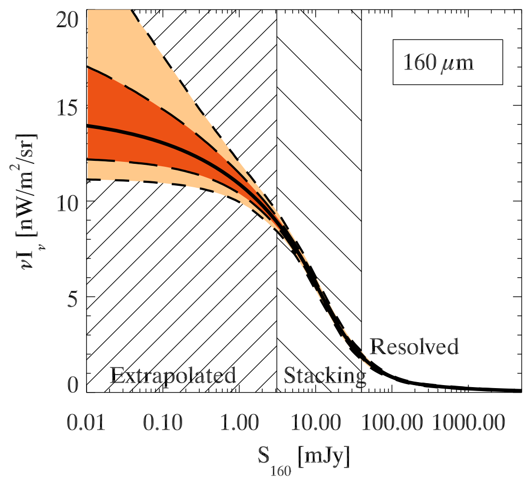

Fig. 11. Cumulative contribution to the surface brightness of the 160 μm CIB as a function of $S_{160\,\mu m}$. The colored area represents the 68% and 95% confidence level. The shaded areas represent the $3.1 < S_{160} < 45$ mJy stacking counts zone and the $S_{160} < 3.1$ mJy power-law extrapolation zone (see Sect. 6.2). The 12% calibration uncertainty is not represented. The table corresponding to this figure is available online at http://www.ias.u-psud.fr/irgalaxies/

1.61±0.21 at 160 μm. The slope of the number counts at 70 μm is compatible with the Frayer et al. (2006) value (1.63 ± 0.34). The slope at 160 μm is measured for the first time. Our new estimate of the CIB at 70 μm and 160 μm due to infrared galaxies is thus $6.6^{+0.7}_{-0.6}$ nW m^{-2} sr^{-1}, and $14.6^{+7.1}_{-2.9}$ nW m^{-2} sr^{-1}, respectively. We conclude that resolved and stacking-studied populations account for 82% and 62% of the CIB at 70 μm and 160 μm, respectively. These results are summarized in Table 7, and Figs. 10 and 11.

7. Discussion

7.1. New lower limits of the CIB

The estimations of CIB based on number counts ignore a potential diffuse infrared emission like dust in galaxy clusters (Montier & Giard 2005). The extrapolation of the faint source counts supposes no low luminosity population, like population III stars or faint unseen galaxies. Accordingly, this type of measurement can provide in principle only a lower limit.

At 24 μm, Papovich et al. (2004) found $2.7^{-0.7}_{1.1}$ nW m^{-2} sr^{-1} using the counts and the extrapolation of the faint source counts. We agree with this work and significantly reduced the uncertainties on this estimation. Dole et al. (2006) found a contribution of 1.93 ± 0.23 nW m^{-2} sr^{-1} for $S_{24} > 60$ μJy sources (after dividing their results by 1.12 to correct an aperture error in their photometry at 24 μm). Our analysis gives 2.10 ± 0.08 nW m^{-2} sr^{-1} for a cut at 60 μJy, which agrees very well. Rodighiero et al. (2006) gave a total value of 2.6 nW m^{-2} sr^{-1}, without any error bar. Chary et al. (2004) found 2.0 ± 0.2 nW m^{-2} sr^{-1}, by integrating sources between 20 and 1000 μJy (we find 2.02 ± 0.10 for the same interval).

At 70 μm, using the number counts in the ultra deep GOODS-N and a P(D) analysis, Frayer et al. (2006) found a $S_{70} > 0.3$ mJy source contribution to the 70 μm CIB of 5.5 ± 1.1 nW m^{-2} sr^{-1}. Using the stacking counts, we found 5.5 ± 0.4 nW m^{-2} sr^{-1} for the same cut, in excellent agreement and with improved uncertainties. In Dole et al. (2006), the contribution at 70 μm of the $S_{24} < 60$ μJy sources was computed with an extrapolation of the 24 μm number counts and the 70/24 color. They found 7.1 ± 1.0 nW m^{-2} sr^{-1}, but the uncertainty on the extrapolation took only into account the uncertainty on the 70/24 color and not the uncertainty on the extrapolated 24 μm contribution, and was thus slightly underestimated. This is in agrees with our estimation.

At 160 μm they found with the same method, 17.4 ± 2.1 nW m^{-2} sr^{-1} (a corrective factor of 1.3 was applied due to an error on the map pixel size). This estimation is a little bit higher than our estimation, and can be explained by a small contribution (of the order of 15%) of the source clustering (Bavouzet 2008).

Our results can also be compared with direct measurements made by absolute photometers. These methods are biased by the foreground modeling, but do not ignore the extended emission. Fixsen et al. (1998) found a CIB brightness of 13.7 ± 3.0 at 160 μm, in excellent agreement with our estimation ($14.6^{+7.1}_{-2.9}$ nW m^{-2}). From the discussion in Dole et al. (2006) (Sect. 4.1), the Lagache et al. (2000) DIRBE WHAM (FIRAS calibration) estimation at 140 μm and 240 μm of 12 nW m^{-2} sr^{-1} and 12.2 nW m^{-2} sr^{-1} can be also compared with our value at 160 μm. A more recent work of Odegard et al. (2007) found 25.0 ± 6.9 and 13.6 ± 2.5 nW m^{-2} sr^{-1} at 140 μm and 240 μm respectively (resp. 15 ± 5.9 nW m^{-2} sr^{-1} and 12.7 ± 1.6 nW m^{-2} sr^{-1} with the FIRAS scale). Using ISOPHOT data, Juvela et al. (2009) give an estimation of the CIB surface brightness between 150 μm and 180 μm of $20.25 \pm 6.0 \pm 5.6$ nW m^{-2} sr^{-1}.

The total brightness due to infrared galaxies at 160 μm corresponds to the total CIB level at this wavelength. We thus have probably resolved the CIB at this wavelength. Nevertheless, the uncertainties are relatively large, and other minor CIB contributors cannot be excluded.

In addition, upper limits can be deduced indirectly from blazar high energy spectrum. Stecker & de Jager (1997) gave an upper limit of 4 nW m^{-2} sr^{-1} at 20 μm using Mkn 421. Renault et al. (2001) found an upper limit of 4.7 nW m^{-2} sr^{-1} between 5 and 15 μm with Mkn 501. This is consistent with our lower limit at 24 μm.

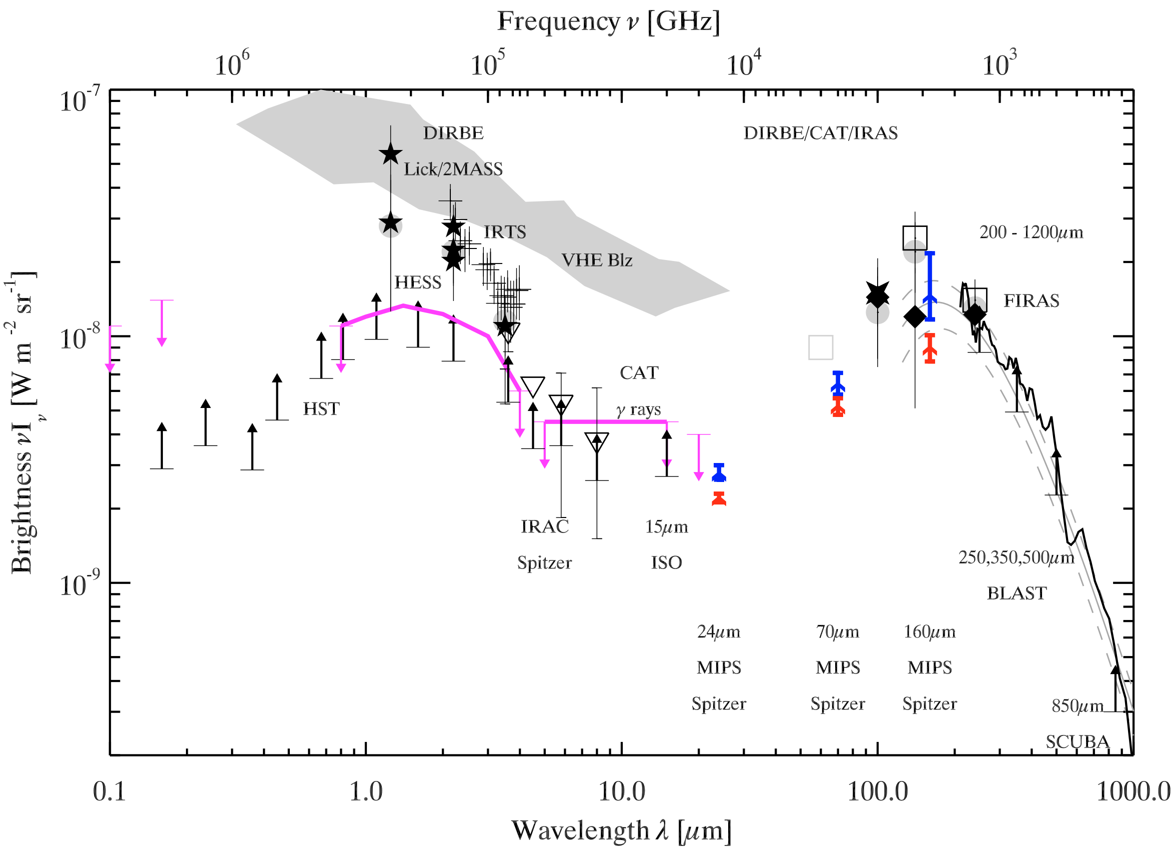

Fig. 12. Current measurement of the extragalactic background light spectral energy distribution from 100 nm to 1mm, with the cosmic optical background (COB, $\lambda < 8\,\mu$m) and cosmic infrared background (CIB, $\lambda > 8\,\mu$m). Our new points at 24 μm, 70 μm and 160 μm are plotted (*triangle*). Lower (red) triangles correspond to the CIB resolved with the number counts and stacking counts. Upper (blue) triangles correspond to the total extrapolated CIB due to infrared galaxies. BLAST lower limits at 250 μm, 350 μm and 500 μm (Devlin et al. 2009; Marsden et al. 2009) are represented in *black arrows*. The FIRAS measurements of Fixsen et al. (1998) between 125 μm and 2000 μm are plotted with a *grey solid line*, and the 1-σ confidence region with a *grey dashed line*. Other points come from different authors (see Dole et al. (2006) for complete details). Old MIPS points are not plotted for clarity.

An update of the synthetic EBL SED of Dole et al. (2006) with the new BLAST (balloon-borne large-aperture submillimeter telescope) lower limits from Devlin et al. (2009) and our values is plotted in Fig. 12. The BLAST lower limits are obtained by stacking of the Spitzer 24 μm sources at 250 μm, 350 μm and 500 μm (Devlin et al. 2009; Marsden et al. 2009).

7.2. 160 μm number counts

At most, we observed a 30% overestimation of the Lagache et al. (2004) model compared to the 160 μm number counts (Sect. 4.4 and 5.3 and Fig. 7), despite good fits at other wavelengths. This model uses mean SEDs of galaxies sorted into two populations (starburst and cold), whose luminosity functions evolve separately with the redshift. A possible explanation of the model excess is a slightly too high density of local cold galaxies. By decreasing the density of this local population a little, the model might be able to better fit the 160 μm number counts without significantly affecting other wavelengths, especially at 70 μm (more sensitive to warm dust rather than cold dust), and in the submillimetre range (more sensitive to redshifted cold dust at faint flux densities for wavelengths larger than 500 μm).

The Le Borgne et al. (2009) model slightly overpredicts faint 160 μm sources, probably because of the presence of too many galaxies at high redshift; this trend is also seen at 70 μm. With our number counts as new constraints, their inversion should give more accurate parameters.

Herschel was successfully launched on May 14th, 2009 (together with *Planck*). It will observe infrared galaxies between 70 μm and 500 μm with an improved sensitivity. It will be possible to directly observe the cold dust spectrum of high-z ULIRG (ultra luminous infrared galaxy) and medium-z LIRG (luminous infrared galaxy). PACS (Photodetectors Array Camera and Spectrometer) will make photometric surveys in three bands centred on 70 μm, 100 μm and 160 μm. *Herschel* will allow us to resolve a significant fraction of the background at these wavelengths (Lagache et al. 2003; Le Borgne et al. 2009). SPIRE (spectral and photometric imaging receiver) will observe around 250 μm, 350 μm and 500 μm, and will be quickly confusion limited. In both cases, the stacking analysis will allow us to probe fainter flux density levels, as it is complementary to *Spitzer* and BLAST.

8. Conclusion

With a large sample of public *Spitzer* extragalactic maps, we built new deep, homogeneous, high-statistics number counts in three MIPS bands at 24 μm, 70 μm and 160 μm.

At 24 μm, the results agree with previous works. These counts are derived from the widest surface ever used at this wavelength (53.6 deg^2). Using these counts, we give an accurate estimation of the galaxy contribution to the CIB at this wavelength ($2.86^{+0.19}_{-0.16}$ nW m^{-2} sr^{-1}).

At 70 μm, we used the stacking method to determine the counts below the detection limit of individual sources, by reaching 0.38 mJy, allowing us to probe the faint flux density slope of differential number counts. With this information, we deduced the total contribution of galaxies to the CIB at this wavelength ($6.6^{+0.7}_{-0.6}$ nW m^{-2} sr^{-1}).

At 160 μm, our counts reached 3 mJy with a stacking analysis. We exhibited for the first time the maximum in differential number counts around 20 mJy and the power-law behavior below 10 mJy. We deduced the total contribution of galaxies to the CIB at this wavelength ($14.6^{+7.1}_{-2.9}$ nW m^{-2} sr^{-1}). *Herschel* will likely probe flux densities down to about 10 mJy at this wavelength (confusion limit, Le Borgne et al. (2009)).

The uncertainties on the number counts used in this work take carefully into account the galaxy clustering, which is measured with the "counts-in-cells" method.

We presented a method to build very deep number counts with the information provided by shorter wavelength data (MIPS 24 μm) and a stacking analysis. This tool could be used on *Herschel* SPIRE data with a PACS prior to probe fainter flux densities in the submillimetre range.

We publicly release on the website `http://www.ias.u-psud.fr/irgal/`, the following products: PSF, number counts and CIB contributions. We also release a stacking library software written in IDL.

Acknowledgements. We wish to acknowledge G. Lagache, who has generated simulations used in this work. We acknowledge J.L. Puget, G. Lagache, D. Marcillac, B. Bertincourt, A. Penin and all members of the cosmology group of IAS for their comments and suggestions. We wish to thank the members of ANR D-SIGALE for their valuable comments, in particular D. Le Borgne for providing us an electronic version of his model. We also thank E. Le Floc'h for quickly providing us the table of his counts. This work is based in part on archival data obtained with the Spitzer Space Telescope, which is operated by the Jet Propulsion Laboratory, California Institute of Technology under a contract with NASA. Support for this work was provided by an award issued by JPL/Caltech. This publication makes use of data products from the Two Micron All Sky Survey, which is a joint project of the University of Massachusetts and the Infrared Processing and Analysis Center/California Institute of Technology, funded by the National Aeronautics and Space Administration and the National Science Foundation.

Appendix A: Uncertainties on number counts including clustering

A.1. Counts-in-cells moments

We consider a clustered population with a surface density ρ. The expected number of objects in a field of the size Ω is $\overline{N} = \rho\Omega$. In the Poissonian case, the standard deviation around this value is $\sqrt{N}$. For a clustered distribution, the standard deviation σ_N is given by (Wall & Jenkins 2003)

$$\sigma_N = \sqrt{y.\bar{N}^2 + \bar{N}}. \tag{A.1}$$

The expected value of y is given by (Peebles 1980)

$$y = \frac{\int_{\rm field}\int_{\rm field} w(\theta)\mathrm{d}\Omega_1\mathrm{d}\Omega_2}{\Omega^2}, \tag{A.2}$$

where $w(\theta)$ is the angular two points auto correlation function of the sources.

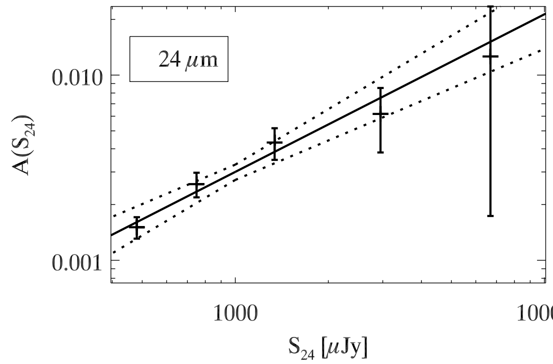

Fig. A.1. Amplitude of the auto correlation as a function of the flux density of the sources at 24 μm, and best power-law fit.

A.2. Measuring source clustering as a function of flux density

We assume the classical power law description $w(\theta) = A(S,\lambda)\theta^{1-\gamma}$ with an index $\gamma = 1.8$. So, y depends only on A and on the shape of the field:

$$y = A(S,\lambda)\frac{\int_{\rm field}\int_{\rm field}\theta^{1-\gamma}\mathrm{d}\Omega_1\mathrm{d}\Omega_2}{\Omega^2}. \tag{A.3}$$

The uncertainty on y is given by (Szapudi 1998):

$$\sigma_y = \sqrt{\frac{2}{N_{\rm cell}\bar{N}^2}}. \tag{A.4}$$

To measure $A(S,\lambda)$, we cut our fields in $30'\times30'$ square boxes, in which we count the number of sources and compute the variance in five, three and three flux density bins at 24 μm, 70 μm and 160 μm. We calculate the associate $A(S,\lambda)$ combining Eqs. (A.1) and (A.3)

$$A(S,\lambda) = \frac{\sigma_N^2 - \bar{N}}{\bar{N}^2} \times \frac{\Omega^2}{\int_{\rm field}\int_{\rm field}\theta^{1-\gamma}\mathrm{d}\Omega_1\mathrm{d}\Omega_2}. \tag{A.5}$$

The fit of $A(S_{24}, 24\ \mu\mathrm{m})$ versus S_{24} (see Fig. A.1) gives ($\chi^2 = 2.67$ for five points and two fitted parameters)

$$A(S, 24\ \mu\mathrm{m}) = (2.86 \pm 0.29)\times10^{-3}\left(\frac{S}{1\ \mathrm{mJy}}\right)^{0.90\pm0.15}. \tag{A.6}$$

The measured exponent in A.6 of 0.90 ± 0.15 corresponds to $\gamma/2$, which is the expected value in the case of a flux-limited survey in an Euclidean universe filled with single luminosity sources. We fix this exponent to fit $A(S_{70}, 70\ \mu$m) and $A(S_{160}, 160\ \mu$m). We find $A(1$ mJy, 70 μm$) = (0.25 \pm 0.08).10^{-3}$ and $A(1$ mJy, 160 μm$) = (0.3 \pm 0.03).10^{-3}$.

A.3. Compute uncertainties due to clustering

With this model of $A(S,\lambda)$ and the field shape, we compute y (Eq. (A.3)). Assuming $\bar{N} = N$ (N to be the number of detected sources in a given field and flux density bin), we deduce $\sigma(N)$ from Eq. (A.1), and consequently the error bar on the number counts for a single field.

To compute the final uncertainty on the combined counts, we use the following relation

$$\sigma_{{\rm comb},\frac{dN}{dS}} = \frac{\sqrt{\sum_i \Omega_i^2\sigma^2_{i,\frac{dN}{dS}}}}{\sum_i \Omega_i}, \tag{A.7}$$

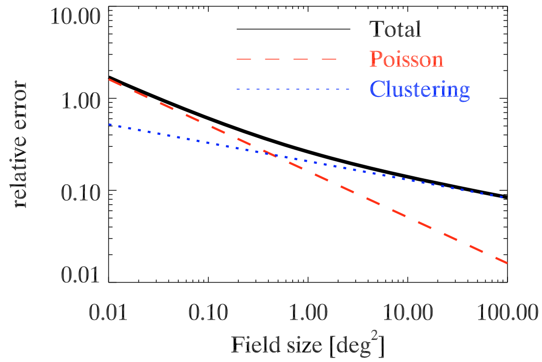

Fig. A.2. Relative error on the number count as a function of the field size. We have chosen $A = 0.019$ and $\rho = 38.5$ deg^{-2} (values for a 80–120 mJy flux density bin at 160 μm). The field is a square.

where $\sigma_{\mathrm{comb},\frac{\mathrm{d}N}{\mathrm{d}S}}$ is the uncertainty on the combined number counts, Ω_i the solid angle of the ith field, and $\sigma_{i,\frac{\mathrm{d}N}{\mathrm{d}S}}$ the uncertainty on the number counts in the ith field (given by Var(N), Eq. (A.1)).

A.4. Discussion about clustering and number count uncertainties

For a clustered distribution of sources, the uncertainties on the number counts are driven by two quadratically combined terms (Eq. (A.1)): a Poissonian term $\sqrt{N}$ and a clustering term $\sqrt{y}.N$ (see Fig. A.2). We have $N \propto \Omega$ and $y \propto \Omega^{(\gamma-1)/2}$ (Blake & Wall 2002). When the uncertainty is dominated by the Poissonian term (small field), the relative uncertainty is thus proportional to $\sqrt{\Omega}^{-1/2}$. When the uncertainty is dominated by the clustering term (large field), the relative error is proportional to $\Omega^{(1-\gamma)/4}$ ($\Omega^{-0.2}$ for $\gamma = 1.8$).

Consequently uncertainties decrease very slowly in the the clustering regime. Averaging many small independent fields gives more accurate counts than a big field covering the same surface. For example, in the clustering regime, if a field of 10 deg^2 has a relative uncertainty of 0.2, the relative uncertainty is $0.2/\sqrt{10} = 0.063$ for the mean of ten fields of this size, and $0.2 \times 10^{-0.2} = 0.126$ for a single field of 100 deg^2. Consequently, if one studies the counts only, many small fields give better results than one very large field. But, this is not optimal if one studies the spatial properties of the galaxies, which requires large fields.

References

Arendt, R. G., Odegard, N., Weiland, J. L., et al. 1998, ApJ, 508, 74
Bavouzet, N. 2008, Ph.D. Thesis, Université Paris-Sud 11 http://tel.archives-ouvertes.fr/tel-00363975/
Bertin, E., & Arnouts, S. 1996, A&AS, 117, 393
Blake, C., & Wall, J. 2002, MNRAS, 337, 993
Chary, R., Casertano, S., Dickinson, M. E., et al. 2004, ApJS, 154, 80
Devlin, M. J., Ade, P. A. R., Aretxaga, I., et al. 2009, Nature, 458, 737
Diolaiti, E., Bendinelli, O., Bonaccini, D., et al. 2000, A&AS, 147, 335
Dole, H., Gispert, R., Lagache, G., et al. 2001, A&A, 372, 364
Dole, H., Lagache, G., & Puget, J.-L. 2003, ApJ, 585, 617
Dole, H., Le Floc'h, E., Pérez-González, P. G., et al. 2004, ApJS, 154, 87
Dole, H., Lagache, G., Puget, J.-L., et al. 2006, A&A, 451, 417
Dye, S., Eales, S. A., Ashby, M. L. N., et al. 2006, ApJ, 644, 769
Dye, S., Ade, P. A. R., Bock, J. J., et al. 2009, ApJ, 703, 285
Eddington, A. S. 1913, MNRAS, 73, 359
Eddington, Sir, A. S. 1940, MNRAS, 100, 354
Elbaz, D., Cesarsky, C. J., Chanial, P., et al. 2002, A&A, 384, 848
Engelbracht, C. W., Blaylock, M., Su, K. Y. L., et al. 2007, PASP, 119, 994
Fernandez-Conde, N., Lagache, G., Puget, J.-L., & Dole, H. 2008, A&A, 481, 885
Fixsen, D. J., Dwek, E., Mather, J. C., Bennett, C. L., & Shafer, R. A. 1998, ApJ, 508, 123
Franceschini, A., Rodighiero, G., Vaccari, M., Marchetti, L., & Mainetti, G. 2010, A&A, accepted [arXiv:0906.4264]
Frayer, D. T., Huynh, M. T., Chary, R., et al. 2006, ApJ, 647, L9
Frayer, D. T., Sanders, D. B., Surace, J. A., et al. 2009, AJ, 138, 1261
Gispert, R., Lagache, G., & Puget, J. L. 2000, A&A, 360, 1
Gordon, K. D., Engelbracht, C. W., Fadda, D., et al. 2007, PASP, 119, 1019
Hauser, M. G., & Dwek, E. 2001, ARA&A, 39, 249
Hauser, M. G., Arendt, R. G., Kelsall, T., et al. 1998, ApJ, 508, 25
Juvela, M., Mattila, K., Lemke, D., et al. 2009, A&A, 500, 763
Kashlinsky, A. 2005, Phys. Rep., 409, 361
Krist, J. 2006, Tiny Tim/Spitzer User's Guide
Lagache, G., Abergel, A., Boulanger, F., Désert, F. X., & Puget, J.-L. 1999, A&A, 344, 322
Lagache, G., Haffner, L. M., Reynolds, R. J., & Tufte, S. L. 2000, A&A, 354, 247
Lagache, G., Dole, H., & Puget, J.-L. 2003, MNRAS, 338, 555
Lagache, G., Dole, H., Puget, J.-L., et al. 2004, ApJS, 154, 112
Lagache, G., Puget, J.-L., & Dole, H. 2005, ARA&A, 43, 727
Le Borgne, D., Elbaz, D., Ocvirk, P., & Pichon, C. 2009, A&A, 504, 727
LeFloc'h, E., Aussel, H., Ilbert, O., et al. 2009, ApJ, 703, 222
Marsden, G., Ade, P. A. R., Bock, J. J., et al. 2009, ApJ, 707, 1729
Montier, L. A., & Giard, M. 2005, A&A, 439, 35
Odegard, N., Arendt, R. G., Dwek, E., et al. 2007, ApJ, 667, 11
Papovich, C., Dole, H., Egami, E., et al. 2004, ApJS, 154, 70
Pascale, E., Ade, P. A. R., Bock, J. J., et al. 2009, ApJ, 707, 1740
Pearson, C., & Khan, S. A. 2009, MNRAS, 399, L11
Peebles, P. J. E. 1980, The large-scale structure of the universe
Puget, J.-L., Abergel, A., Bernard, J.-P., et al. 1996, A&A, 308, L5
Renault, C., Barrau, A., Lagache, G., & Puget, J.-L. 2001, A&A, 371, 771
Rieke, G. H., Young, E. T., Engelbracht, C. W., et al. 2004, ApJS, 154, 25
Rodighiero, G., Lari, C., Pozzi, F., et al. 2006, MNRAS, 371, 1891
Rowan-Robinson, M. 2009, MNRAS, 394, 117
Serjeant, S., Mortier, A. M. J., Ivison, R. J., et al. 2004, ApJS, 154, 118
Shupe, D. L., Rowan-Robinson, M., Lonsdale, C. J., et al. 2008, AJ, 135, 1050
Skrutskie, M. F., Cutri, R. M., Stiening, R., et al. 2006, AJ, 131, 1163
Stansberry, J. A., Gordon, K. D., Bhattacharya, B., et al. 2007, PASP, 119, 1038
Starck, J. L., Aussel, H., Elbaz, D., Fadda, D., & Cesarsky, C. 1999, A&AS, 138, 365
Stecker, F. W., & de Jager, O. C. 1997, ApJ, 476, 712
Stetson, P. B. 1987, PASP, 99, 191
Szapudi, I. 1998, ApJ, 497, 16
Valiante, E., Lutz, D., Sturm, E., Genzel, R., & Chapin, E. 2009, ApJ, 701, 1814
Wall, J. V., & Jenkins, C. R. 2003, Practical Statistics for Astronomers
Wang, W.-H., Cowie, L. L., & Barger, A. J. 2006, ApJ, 647, 74
Werner, M. W., Gallagher, D. B., & Irace, W. R. 2004, Adv. Space Res., 34, 600

5.4 Article : *Submillimeter number counts at 250 μm, 350 μm and 500 μm in BLAST data*

Les résultats présentés Chap. 2, 3 et 5 et concernant les comptages de sources et le CIB dans les bandes BLAST ont été publiés dans le journal *Astronomy&Astrophysics*.

A&A 516, A43 (2010)
DOI: 10.1051/0004-6361/200913910

Astronomy & Astrophysics

Submillimeter number counts at 250 μm, 350 μm and 500 μm in BLAST data

M. Béthermin, H. Dole, M. Cousin, and N. Bavouzet

Institut d'Astrophysique Spatiale (IAS), Université Paris-Sud 11 and CNRS (UMR8617), Bât. 121, 91405 Orsay, France
e-mail: matthieu.bethermin@ias.u-psud.fr

Received 18 December 2009 / Accepted 6 March 2010

ABSTRACT

Context. The instrument BLAST (Balloon-borne Large-Aperture Submillimeter Telescope) performed the first deep and wide extragalactic survey at 250, 350 and 500 μm. The extragalactic number counts at these wavelengths are important constraints for modeling the evolution of infrared galaxies.

Aims. We estimate the extragalactic number counts in the BLAST data, which allow a comparison with the results of the P(D) analysis of Patanchon et al. (2009).

Methods. We use three methods to identify the submillimeter sources. 1) Blind extraction using an algorithm when the observed field is confusion-limited and another one when the observed field is instrumental-noise-limited. The photometry is computed with a new simple and quick point spread function (PSF) fitting routine (FASTPHOT). We use Monte-Carlo simulations (addition of artificial sources) to characterize the efficiency of this extraction, and correct the flux boosting and the Eddington bias. 2) Extraction using a prior. We use the *Spitzer* 24 μm galaxies as a prior to probe slightly fainter submillimeter flux densities. 3) A stacking analysis of the *Spitzer* 24 μm galaxies in the BLAST data to probe the peak of the differential submillimeter counts.

Results. With the blind extraction, we reach 97 mJy, 83 mJy and 76 mJy at 250 μm, 350 μm and 500 μm respectively with a 95% completeness. With the prior extraction, we reach 76 mJy, 63 mJy, 49 mJy at 250 μm, 350 μm and 500 μm respectively. With the stacking analysis, we reach 6.2 mJy, 5.2 mJy and 3.5 mJy at 250 μm, 350 μm and 500 μm respectively. The differential submillimeter number counts are derived, and start showing a turnover at flux densities decreasing with increasing wavelength.

Conclusions. There is a very good agreement with the P(D) analysis of Patanchon et al. (2009). At bright fluxes (>100 mJy), the Lagache et al. (2004) and Le Borgne et al. (2009) models slightly overestimate the observed counts, but the data agree very well near the peak of the differential number counts. Models predict that the galaxy populations probed at the peak are likely $z \sim 1.8$ ultra-luminous infrared galaxies.

Key words. cosmology: observations – galaxies: statistics – galaxies: evolution – galaxies: photometry – infrared: galaxies

1. Introduction

Galaxy number counts, a measurement of the source surface density as a function of flux density, are used to evaluate the global evolutionary photometric properties of a population observed at a given wavelength. These photometric properties mainly depend on the source redshift distribution, spectral energy distribution (SED), and luminosity distribution in a degenerate way for a given wavelength. Even though this is a rather simple tool, measurements of number counts at different observed wavelengths greatly help in constraining those degeneracies. Backward evolution models, among these Chary & Elbaz (2001); Lagache et al. (2004); Gruppioni et al. (2005); Franceschini et al. (2009); Le Borgne et al. (2009); Pearson & Khan (2009); Rowan-Robinson (2009); Valiante et al. (2009) are able to broadly reproduce (with different degrees of accuracy) the observed number counts from the near-infrared to the millimeter spectral ranges, in addition to other current constraints, like such as measured luminosity functions and the spectral energy distribution of the Cosmic Infrared Background (CIB) (Puget et al. 1996; Fixsen et al. 1998; Hauser et al. 1998; Lagache et al. 1999; Gispert et al. 2000; Hauser & Dwek 2001; Kashlinsky 2005; Lagache et al. 2005; Dole et al. 2006). In the details, however, the models disagree in some aspects like the relative evolution of luminous and ultra-luminous infrared galaxies (LIRG and ULIRG) and their redshift distributions, or the mean temperature or colors of galaxies, as is shown for instance in LeFloc'h et al. (2009) from Spitzer 24 μm deep observations.

One key spectral range lacks valuable data to get accurate constraints as yet: the sub-millimeter range, between 160 μm and 850 μm, where some surveys were conducted on small areas. Fortunately this spectral domain is intensively studied with the BLAST balloon experiment (Devlin et al. 2009) and the *Herschel* and *Planck* space telescopes. This range, although it is beyond the maximum of the CIB's SED in wavelength, allows us to constrain the poorly-known cold component of galaxy SED at a redshift greater than a few tenths. Pioneering works have measured the local luminosity function (Dunne et al. 2000) and shown that most milli-Jansky sources lie at redshifts $z > 2$ (Ivison et al. 2002; Chapman et al. 2003a, 2005; Ivison et al. 2005; Pope et al. 2005, 2006). Other works showed that the galaxies SED selected in the submillimeter range (Benford et al. 1999; Chapman et al. 2003b; Sajina et al. 2003; Lewis et al. 2005; Beelen et al. 2006; Kovács et al. 2006; Sajina et al. 2006; Michałowski et al. 2010) can have typically warmer temperatures and higher luminosities than galaxies selected at other infrared wavelengths.

Data in the submillimeter wavelength with increased sensitivity are thus needed to match the depth of infrared surveys, conducted by Spitzer in the mid- and far-infrared with the MIPS instrument (Rieke et al. 2004) at 24 μm, 70 μm and 160 μm (Chary et al. 2004; Marleau et al. 2004; Papovich et al. 2004; Dole et al. 2004; Frayer et al. 2006a,b; Rodighiero et al. 2006; Shupe et al. 2008; Frayer et al. 2009; LeFloc'h et al. 2009; Béthermin et al. 2010) as well as the near-infrared range with the IRAC instrument (Fazio et al. 2004b) between 3.6 μm and 8.0 μm (Fazio et al. 2004a; Franceschini et al. 2006; Sullivan et al. 2007; Barmby et al. 2008; Magdis et al. 2008; Ashby et al. 2009). Infrared surveys have allowed the resolution of the CIB by identifying the contributing sources – directly at 24 μm and 70 μm, or indirectly trough stacking at 160 μm (Dole et al. 2006; Béthermin et al. 2010).

Although large surveys cannot solve by themselves all the unknowns about the submillimeter SED of galaxies, the constraints given by the number counts can greatly help in unveiling the statistical SED shape of submillimeter galaxies as well as the origin of the submillimeter background.

The instrument BLAST (Balloon-borne Large-Aperture Submillimeter Telescope, Pascale et al. 2008) performed the first wide and deep survey in the 250–500 μm range (Devlin et al. 2009) before the forthcoming *Herschel* results. Marsden et al. (2009) show that sources detected by *Spitzer* at 24 μm emit the main part of the submillimeter background. Khan et al. (2009) claimed that only 20% of the CIB is resolved by the sources brighter than 17 mJy at 350 μm. Patanchon et al. (2009) has performed a $P(D)$ fluctuation analysis to determine the counts at BLAST wavelength (250 μm, 350 μm and 500 μm). In this paper we propose another method to estimate the number counts at these wavelengths and compare the results with those of Patanchon et al. (2009).

2. Data

2.1. BLAST sub-millimeter public data in the Chandra Deep Field South (CDFS)

The BLAST holds a bolometer array, which is the precursor of the spectral and photometric imaging receiver (SPIRE) instrument on *Herschel*, at the focus of a 1.8 m diameter telescope. It observes at 250 μm, 350 μm and 500 μm, with a 36″, 42″ and 60″ beam, respectively (Truch et al. 2009).

An observation of the Chandra Deep Field South (CDFS) was performed during a long duration flight in Antarctica in 2006, and the data of the two surveys are now public: a 8.7 deg^2 shallow field and a 0.7 deg^2 confusion-limited (Dole et al. 2004) field in the center part of the first one. We use the non-beam-smoothed maps and associated point spread function (PSF) distributed on the BLAST website[1]. The signal and noise maps were generated by the SANEPIC algorithm (Patanchon et al. 2008).

2.2. Spitzer 24 μm data in the CDFS

Several infrared observations were performed in the CDFS. The *Spitzer* Wide-Field InfraRed Extragalactic (SWIRE) survey overlaps the CDFS BLAST field at wavelengths between 3.6 μm and 160 μm. We used only the 24 μm band, which is 80% complete at 250 μJy. The completeness is defined as the probability to find a source of a given flux in a catalog. The Far-Infrared Deep Extragalactic Legacy (FIDEL) survey is deeper but narrower (about 0.25 deg^2) than SWIRE and 80% complete at 57 μJy at 24 μm. We used the Béthermin et al. (2010) catalogs constructed from these two surveys. These catalogs were extracted with SExtractor (Bertin & Arnouts 1996) and the photometry was performed with the allstar routine of the DAOPHOT package (Stetson 1987). The completeness of this catalog was characterized with Monte-Carlo simulations (artificial sources added on the initial map and extracted).

[1] http://www.blastexperiment.info

3. Blind source extraction and number counts

We started with a blind source extraction in the BLAST bands. Each wavelength was treated separately. For each wavelength we defined two masks: a shallow zone (about 8.2 deg^2) covering the whole field except the noisier edge; and a deep zone (about 0.45 deg^2) in the center of the confusion-limited area. We used different extraction methods in the shallow zone and the deep one, but the photometry and the corrections of the extraction bias were the same.

3.1. Detector noise-limited extraction (shallow zone)

In the shallow zone we used the non-smoothed map and the corresponding map of the standard deviation of the noise. The map was then cross-correlated by the PSF. The result of this cross-correlation is

$$m_{\rm conv}(i_0, j_0) = \sum_{i=-N}^{+N} \sum_{j=-N}^{+N} m(i_0+i, j_0+j) \times PSF(i,j), \qquad (1)$$

where $m_{\rm conv}(i_0, j_0)$ is the flux density in the pixel (i_0, j_0) of the cross-correlated map, $m(i, j)$ the flux density in the pixel (i, j) of the map, and PSF(i, j) the value of the normalized PSF in the pixel (i, j) (the center of the PSF is in the center of the pixel $(0, 0)$). The PSF size is $(2N + 1)\times(2N + 1)$ pixels. The standard deviation of the noise in the cross-correlated map is thus

$$n_{\rm conv}(i_0, j_0) = \sqrt{\sum_{i=-N}^{+N} \sum_{j=-N}^{+N} n^2(i_0+i, j_0+j) \times PSF^2(i,j)}, \qquad (2)$$

where n ($n_{\rm conv}$) is the initial (cross-correlated) map of the standard deviation of the noise.

We found the pixels where $m_{\rm conv}/n_{\rm conv} > 3$ and kept the local maxima. The precise center of the detected sources was computed by a centroid algorithm. This low threshold caused lots of spurious detections, but helped to deblend the fluxes of 3 to 4-sigma sources and avoided to overestimate their fluxes. We could thus limit the flux boosting effect. A final cut in flux after the PSF fitting photometry eliminated the main part of these sources. We performed the extraction algorithm on the flipped map (initial map multiplied by a factor of –1) to check it. We found few spurious sources brighter than the final cut in flux determined in the Sect. 3.4. We found a spurious rate of 12%, 11% and 25% at 250 μm, 350 μm and 500 μm, respectively.

3.2. Confusion-limited extraction (deep zone)

In the confusion-limited zone we also used a non-smoothed map. In this region the noise is dominated by the confusion and not by the instrumental noise. Consequently, the method based on instrumental noise presented in the Sect. 3.1 is not relevant. We used an atrou wavelet filtering (Starck et al. 1999; Dole et al. 2001) to remove fluctuations at scales larger than 150″. Then we divided the resulting map by $\sigma_{\rm filtered\ map}$, which is the standard

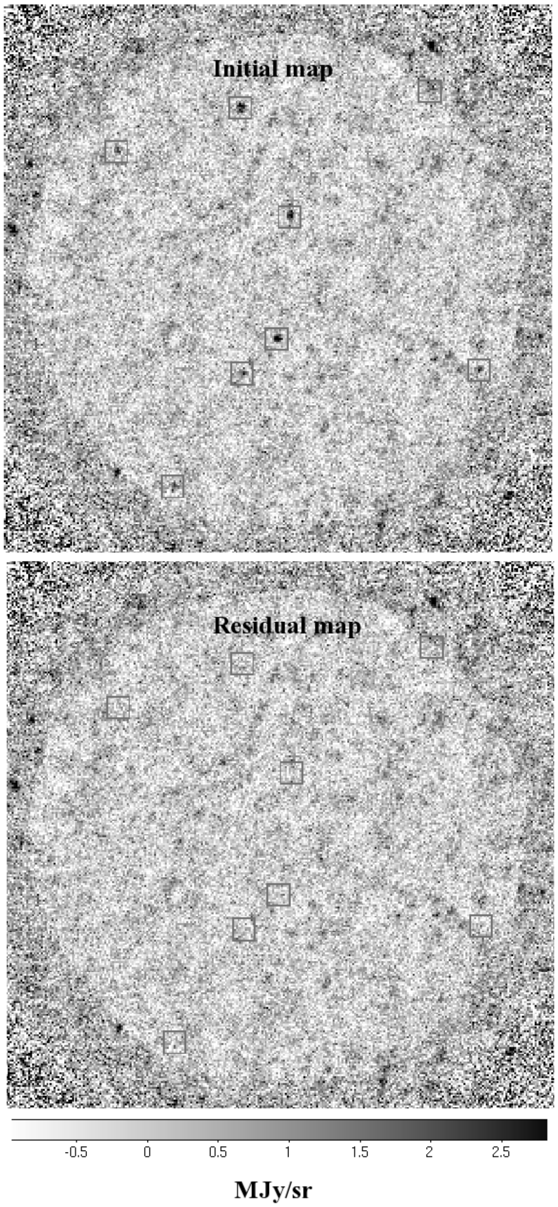

Fig. 1. Position of sources brighter than the 95% completeness flux at 250 μm in deep zone. *Top*: initial map. *Bottom*: residual map. The area out of the mask are represented darker. These 1°×1° map are centered on the coordinates (RA, Dec) = (3h32min30s, –27°50′). The horizontal axis is aligned with the right ascension.

deviation of the pixel values on the filtered map in the working area. We finally kept local maxima with a signal greater than 3. The center of the sources was also determined by a centroid algorithm. The initial map and the cleaned map are shown in Fig. 1. When we flip the map, we find no spurious source brighter than the final cut in flux determined in Sect. 3.4.

3.3. A simple and quick PSF fitting routine: FASTPHOT

For both noise- and confusion-limited extraction, we apply the same quick and simple PSF fitting routine on the non-beam-smoothed map. This routine fits all the detected sources at the same time and is consequently efficient for deblending (although no source was blended in this case; but source-blending will be an issue for an extraction using a prior, detailed in Sect. 4. We suppose that the noise is Gaussian and the position of sources is known. We then maximize the likelihood

$$L(m|S) = \prod_{\text{pixels}} C(n) \times \exp\left[-\frac{\left(m - \sum_{i=1}^{\text{Nsources}} PSF_{x_i,y_i} \times S_i\right)^2}{2n^2}\right], \quad (3)$$

where m and n are the map and the noise map. PSF_{x_i,y_i} is a unit-flux PSF centered at the position (x_i, y_i), which are the coordinates of the ith source. These coordinates are not necessarily integers. $C(n)$ is a normalization constant and depends only of the value of the noise map. $\boldsymbol{S}$ is a vector containing the flux of the sources.

The value of S, which maximizes the likelihood, satisfies the following linear equation stating that the derivative of the likelihood logarithm equals zero

$$\forall i, 0 = \frac{\partial \log\Big(L(m|S)\Big)}{\partial S_i} = A.S + B, \quad (4)$$

where A is a matrix and B a vector defined by

$$A = (a_{ij}) = -\sum_{\text{pixels}} \frac{PSF_{x_i,y_i} \times PSF_{x_j,y_j}}{n^2} \quad (5)$$

$$B = (b_i) = \sum_{\text{pixels}} \frac{PSF_{x_i,y_i} \times map}{n^2} \cdot \quad (6)$$

To perform this operation fast, we used a 70″ × 70″ (respectively 90″ × 90″ and 110″ × 110″) PSF at 250 μm (respectively 350 μm and 500 μm). This PSF, provided by the BLAST team, is the response for a unit-flux source and takes into account all the filtering effects. We used the conjugate gradient method to solve the Eq. (4) quickly.

This routine was tested with 200 × 200 pixels simulated maps containing 400 sources at a known positions with a beam of 10 pixels $FWHM$. The flux of all sources was perfectly recovered in the case where no noise was added. This routine (FASTPHOT) performs simultaneous PSF fitting photometry of 1000 sources in less than 1 s. It is publicly available[2].

3.4. Completeness and photometric accuracy

The completeness is the probability to detect a source of a given flux density. We measured it with a Monte-Carlo simulation. We added artificial point sources (based on PSF) on the initial map at random positions and performed the same source extraction and photometry algorithm as for the real data. A source was considered to be detected if there was a detection in a 20″ radius around the center of the source. Table 1 gives the 95% completeness flux density (for which 95% of sources at this flux are detected) for different wavelengths and depths.

The photometric noise was estimated with the scatter of the recovered fluxes of artificial sources. We computed the standard deviation of the difference between input and output flux. This measurement includes instrumental and confusion noise ($\sigma_{\text{tot}} = \sqrt{\sigma^2_{\text{instr}} + \sigma^2_{\text{conf}}}$). The results are given in Table 1. In the deep

[2] On the IAS website http://www.ias.u-psud.fr/irgalaxies/

Table 1. 95% completeness flux density and photometric noise for different depths at different wavelengths.

	95% completeness mJy		Instrumental noise mJy		Total photometric noise mJy		Deduced confusion noise mJy	
	Shallow	Deep	Shallow	Deep	Shallow	Deep	Shallow	Deep
250 μm	203	97	37.7	11.1	47.3	24.9	28.6	22.3
350 μm	161	83	31.6	9.3	35.8	20.3	16.8	18.0
500 μm	131	76	20.4	6.0	26.4	17.6	16.7	16.5

Notes. The instrumental noise is given by the noise map. The total photometric noise includes the instrumental and confusion noise and is determined by Monte-Carlo simulations. The confusion noise is computed with the formula $\sigma_{\rm conf} = \sqrt{\sigma_{\rm tot}^2 - \sigma_{\rm instr}^2}$.

area, the photometric uncertainties are thus dominated by the confusion noise. The estimations of the confusion noise between the deep and shallow areas are consistent. It shows the accuracy and the consistency of our method.

Note that the uncertainties on flux densities in the Dye et al. (2009) catalog (based only on instrumental noise) are consequently largely underestimated in the confusion-limited area. Indeed, their 5σ detection threshold (based only on instrumental noise) at 500 μm in the deep zone corresponds to 1.76σ if we also include the confusion noise.

The faint flux densities are overestimated due to the classical flux boosting effect. This bias was measured for all bands for 60 flux densities between 10 mJy and 3 Jy with the results of the Monte-Carlo simulations. The measured fluxes were deboosted with this relation. We cut the catalogs at the 95% completeness flux, where the boosting factor is at the order of 10%. Below this cut, the boosting effect increases too quickly to be safely corrected. We also observed a little underestimation at high flux of 1%, 0.5% and 0.5% at 250 μm, 350 μm and 500 μm. It is due to FASTPHOT, which assumes that the position is perfectly known, which is not true, especially for a blind extraction.

3.5. Number counts

We computed number counts with catalogs corrected for boosting. For each flux density bin we subtracted the number of spurious detections estimated in the Sects. 3.1 and 3.2 to the number of detected sources and divided the number of sources by the size of the bin, the size of the field and the completeness.

We also applied a corrective factor for the Eddington bias. We assumed a distribution of flux densities in $dN/dS \propto S^{-r}$ with $r = 3 \pm 0.5$. This range of possible values for r was estimated considering the Patanchon et al. (2009) counts and the Lagache et al. (2004) and Le Borgne et al. (2009) model predictions. We then randomly kept sources with a probability given by the completeness and added a random Gaussian noise to simulate photometric noise. Finally we computed the ratio between the input and output number of sources in each bin. We applied a correction computed for $r = 3$ to each point. We estimated the uncertainty on this correction with the difference between corrections computed for $r = 2.5$ and $r = 3.5$. This uncertainty was quadratically combined with a Poissonian uncertainty (clustering effects are negligible due to the little number of sources in the map, see Appendix A).

The calibration uncertainty of BLAST is 10%, 12% and 13% at 250 μm, 350 μm and 500 μm respectively (Truch et al. 2009). This uncertainty is combined with other uncertainties on the counts. The results are plotted in Fig. 2 and given in Table 2 and interpreted in Sect. 6.

3.6. Validation

We used simulations to validate our method. We generated 50 mock catalogs based on the Patanchon et al. (2009) counts, and which covered 1 deg^2 each. These sources are spatially homogeneously distributed. We then generated the associated maps at 250 μm. We used the instrumental PSF, and added a Gaussian noise with the same standard deviation as in the deepest part of real map.

We performed an extraction of sources and computed the number counts with the method used in the confusion limited part of the field (Sect. 3.2). We then compared the output counts with the initial counts (Fig. 3). We used two flux density bins: 100–141 mJy and 141–200 mJy. We found no significant bias. The correlation between the two bins is 0.46. The neighbor points are thus not anti-correlated as in the Patanchon et al. (2009) P(D) analysis.

The same verification was done on 20 Fernandez-Conde et al. (2008) simulations (based on the Lagache et al. 2004 model). These simulations include clustering. This model overestimates the number of the bright sources, and the confusion noise is thus stronger. The 95% completeness is then reach at 200 mJy. But there is also a very good agreement between input and output counts in bins brighter than 200 mJy. We found a correlation between two first bins of 0.27.

4. Source extraction using *Spitzer* 24 μm catalog as a prior

In addition to blind source extraction in the BLAST data (Sect. 3) we also performed a source extraction using a prior.

4.1. PSF fitting photometry at the position of the Spitzer 24 μm

The catalogs of infrared galaxies detected by *Spitzer* contain more sources than the BLAST catalog. The 24 μm Spitzer PSF has a Full Width at Half Maximum ($FWHM$) of 6.6″. It is smaller than the BLAST PSF (36″ at 250 μm). Consequently, the position of the Spitzer sources is known with sufficient accuracy when correlating with the BLAST data.

We applied the FASTPHOT routine (Sect. 3.3) at the positions of 24 μm sources. We used the Béthermin et al. (2010) SWIRE catalog cut at $S_{24} = 250$ μJy (80% completeness). In order to avoid software instabilities, we kept in our analysis only the brightest *Spitzer* source in a 20″ radius area (corresponding to 2 BLAST pixels). The corresponding surface density is 0.38,

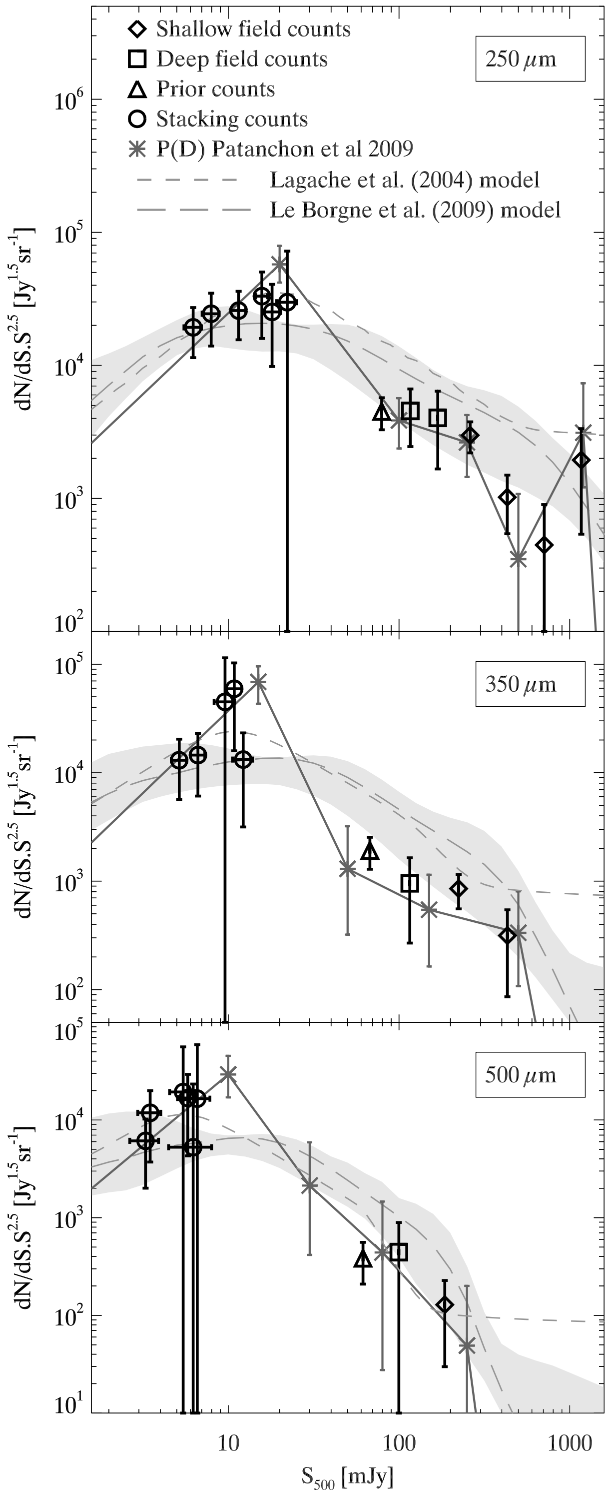

Fig. 2. Extragalactic number counts at 250 μm in the BLAST data. *Diamond*: counts deduced from the source catalog on the whole shallow field; *square*: counts deduced from the catalog of the deep part of the field; *triangle*: counts deduced from catalog of the deep part of the field with a 24 μm prior (this measurement gives only a lower limits to the counts); *cross*: counts computed with a stacking analysis; *grey asterisk*: counts computed with a P(D) analysis by Patanchon et al. (2009); *grey short dashed line*: Lagache et al. (2004) model prediction; *grey long dashed line and grey area*: Le Borgne et al. (2009) model prediction and 1-σ confidence area.

0.49 and 0.89 Spitzer source per beam[3] at 250 μm, 350 μm and 500 μm, respectively.

This method works only if there is no astrometrical offset between the input 24 μm catalog and the BLAST map. We stacked the BLAST sub-map centered on the brightest sources of the SWIRE catalog and measured the centroid of the resulting artificial source. We found an offset of less than 1″. It is negligible compared to the PSF $FWHM$ (36″ at 250 μm).

We worked only in the central region of the deep confusion-limited field (same mask as for blind extraction), where the photometric noise is low.

4.2. Relevance of using Spitzer 24 μm catalog as a prior

The S_{250}/S_{24} (S_{350}/S_{24} or S_{500}/S_{24}) color is not constant, and some sources with a high color ratio could have been missed in the prior catalog (especially high-redshift starbursts). We used the Lagache et al. (2004) and Le Borgne et al. (2009) models to estimate the fraction of sources missed. We selected the sources in the sub-mm flux density bin and computed the 24 μm flux density distribution (see Fig. 4). According to the Lagache et al. (2004) model, 99.6%, 96.4% and 96.9% of the sub-mm selected sources[4] are brighter than $S_{24} = 250\,\mu$Jy for a selection at 250 μm, 350 μm and 500 μm, respectively The Le Borgne et al. (2009) model gives 99.8%, 98.3% and 95.0%, respectively.

4.3. Photometric accuracy

The photometric accuracy was estimated with Monte-Carlo artificial sources. We added five sources of a given flux at random positions on the original map and add them to the 24 μm catalog. We then performed a PSF fitting and compared the input and output flux. We did this 100 times per tested flux for 10 flux densities (between 10 and 100 mJy). In this simulation we assumed that the position of the sources is exactly known. It is a reasonable hypothesis due to the 24 μm PSF $FWHM$ (6.6″) compared to the BLAST one (36″ at 250 μm).

We did not detect any boosting effect for faint flux densities as expected in this case of detection using a prior. For a blind extraction there is a bias of selection toward sources located on peaks of (instrumental or confusion) noise. This is not the case for an extraction using a prior, for which the selection is performed at another wavelength.

The scatter of output flux densities is the same for all the input flux densities. We found a photometric noise σ_S of 21.5 mJy, 18.3 mJy and 16.6 mJy at 250 μm, 350 μm and 500 μm, respectively. It is slightly lower than for the blind extraction, for which the position of source is not initially known.

4.4. Estimation of the number counts

From the catalog described in Sect. 4.1 we give an estimation of the submillimeter number counts at flux densities fainter than reached by the blind-extracted catalog. We cut the prior catalog at 3 σ_S, corresponding to 64 mJy, 54 mJy and 49 mJy at 250 μm, 350 μm and 500 μm, respectively. We worked in a single flux density bin, which is defined to be between this value and the cut of the blind-extracted catalog[4]. There is no flux boosting effect, but we needed to correct the Eddington bias. The completeness

[3] The beam solid angles are taken as 0.39 arcmin^2, 0.50 arcmin^2 and 0.92 arcmin^2 at 250 μm, 350 μm and 500 μm respectively.

[4] The bins are defined as 64 to 97 at 250 μm, 54 to 83 at 350 μm and 49 to 76 at 500 μm.

Table 2. Number counts deduced from source extraction. The not normalized counts can be obtained dividing the $S^{2.5}.\mathrm{d}N/\mathrm{d}S$ column by the S_{mean} column.

Wavelength	S_{mean}	S_{min}	S_{max}	N_{sources}	$S^{2.5}.\mathrm{d}N/\mathrm{d}S$	$\sigma_{S^{2.5}.\mathrm{d}N/\mathrm{d}S}$	Method
μm		mJy		galaxies	gal Jy$^{1.5}$ sr^{-1}		
250	79	64	97	26	4451	1203	Prior
250	116	97	140	5	4529	2090	Deep
250	168	140	203	3	4040	2377	Deep
250	261	203	336	34	2987	784	Shallow
250	430	336	552	5	1023	479	Shallow
250	708	552	910	1	445	449	Shallow
250	1168	910	1500	2	1939	1401	Shallow
350	67	54	83	17	1913	630	Prior
350	115	83	161	2	955	687	Deep
350	223	161	310	16	854	299	Shallow
350	431	310	600	2	314	228	Shallow
500	61	49	76	7	388	178	Prior
500	99	76	131	1	443	448	Deep
500	185	131	262	4	129	99	Shallow

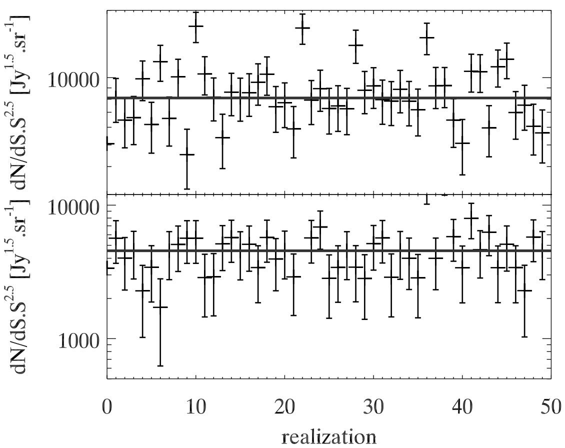

Fig. 3. Number counts at 250 μm deduced from a blind extraction for 50 realizations of a simulation based on the Patanchon et al. (2009) counts. The horizontal *solid line* represents the input count value. The lower panel is the result of the 100–141 mJy bin, the upper panel is the 141–200 mJy bin.

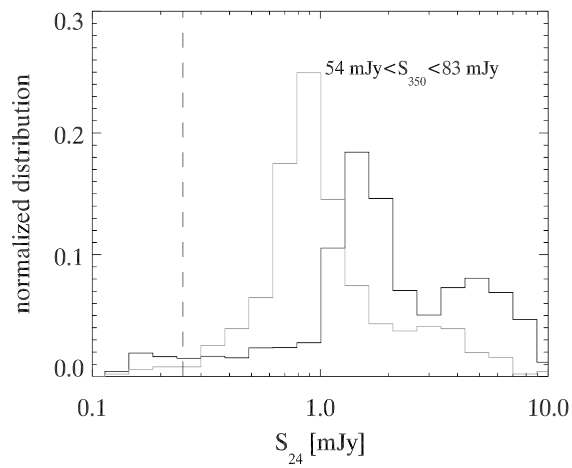

Fig. 4. Flux density distribution at 24 μm of the 54 mJy < S_{350} < 83 mJy sources. The Lagache et al. (2004) model is plotted in *black* and the Le Borgne et al. (2009) model is plotted in *grey*. The *dashed line* represents the cut of our catalog at 24 μm.

could not be defined in the same way as for the blind extraction, because the selection was performed at another wavelength. We thus cannot suppose power-law counts, because the selection function is unknown and the distribution of the extracted sources cannot be computed.

The Eddington bias was estimated with another method. We took the sub-mm flux of each of the sources selected at 24 μm and computed how many sources lie in our count bin. We added a Gaussian noise σ_S to the flux of each source to simulate the photometric errors. We computed the number of sources in the counts bin for the new fluxes. We then compute the mean of the ratio between the input and output number of sources in the selected bin for 1000 realizations. The estimated ratios are 0.42, 0.35 and 0.21 at 250 μm, 350 μm and 500 μm, respectively. These low values indicate that on average the photometric noise introduces an excess of faint sources in our flux bin. This effect is strong because of the steep slope of the number counts, implying more fainter sources than brighter sources. The results are interpreted in the Sect. 6.

4.5. Sub-mm/24 color

In this part we work only on $S > 5\sigma_S$ sources of the catalog described in Sect. 4.1 to avoid bias due to the Eddington bias in our selection. At 250 μm, we have two sources verifying this criterion with a S_{250}/S_{24} color of 16 and 60. No sources are brighter than 5 σ_S at larger wavelengths. For this cut in flux ($S_{250} > 5\sigma_S$), the Lagache et al. (2004) and Le Borgne et al. (2009) models predict a mean S_{250}/S_{24} color of 39 and 41, respectively. The two models predict a mean redshift of 0.8 for this selection, and the K-correction effect explains these high colors.

5. Non-resolved source counts by stacking analysis

5.1. Method

In order to probe the non-resolved source counts, we used same method as Béthermin et al. (2010), i.e. the stacking analysis applied to number counts (hereafter "stacking counts"). We first measured the mean flux at 250 μm, 350 μm or 500 μm as a function of the 24 μm flux ($\overline{S_{250,\ 350\ \mathrm{or}\ 500}} = f(S_{24})$). This measurement was performed by stacking in several S_{24} bins. We used the

Table 3. Number counts deduced from stacking.

Wavelength	S	σ_S	$S^{2.5}.\mathrm{d}N/\mathrm{d}S$	$\sigma_{S^{2.5}.\mathrm{d}N/\mathrm{d}S}$
μm	mJy		gal Jy$^{1.5}$ sr^{-1}	
250	6.2	0.7	19 313	7892
250	7.9	0.9	24 440	10 466
250	11.5	1.2	25 816	10 236
250	15.7	1.3	33 131	17 213
250	18.1	2.3	25 232	15 428
250	22.2	2.9	29 831	42 448
350	5.2	0.5	13007.	7343.
350	6.6	0.6	14519.	8434.
350	10.8	1.2	59314.	43418.
350	9.6	1.3	44944.	69505.
350	12.2	1.6	13200.	10044.
500	3.5	0.5	11842.	8134.
500	3.3	0.6	6115.	4112.
500	5.8	0.8	16789.	12498.
500	5.4	0.9	19338.	36659.
500	6.6	1.2	16526.	42476.
500	6.2	1.8	5263.	18087.

Notes. The not normalized counts can be obtained dividing the $S^{2.5}.\mathrm{d}N/\mathrm{d}S$ column by the S column.

Béthermin et al. (2010) catalog at 24 μm of the FIDEL survey. It is deeper than the SWIRE one used in Sect. 4, but covers a smaller area (0.25 deg^2). The photometry of stacked images was performed with the PSF fitting method (Sect. 3.3), and the uncertainties on the mean flux are computed with a bootstrap method (Bavouzet 2008). We then computed the counts in the sub-mm domain with the following formula:

$$\left.\frac{\mathrm{d}N}{\mathrm{d}S_{\mathrm{submm}}}\right|_{S_{\mathrm{submm}}=f(S_{24})} = \left.\frac{\mathrm{d}N}{\mathrm{d}S_{24}}\right|_{S_{24}} \Big/ \left.\frac{\mathrm{d}S_{\mathrm{submm}}}{\mathrm{d}S_{24}}\right|_{S_{24}}. \quad (7)$$

We show in Appendix B that the clustering effect can be neglected. The results are given in Table 3 and are plotted in Fig. 2.

5.2. Validity of the stacking analysis in the sub-mm range

There are 1.8, 2.4 and 4.5 S_{24} >70 μJy sources per BLAST beam at 250 μm, 350 μm and 500 μm, respectively. We thus stacked several sources per beam. Béthermin et al. (2010) showed that the stacking analysis is valid at 160 μm in the *Spitzer* data, where the size of the beam is similar to the BLAST one.

To test the validity of the stacking analysis in the BLAST data from a *Spitzer* 24 μm catalog, we generated a simulation of a 0.25 deg^2 with a Gaussian noise at the same level as for the real map and with source clustering, following Fernandez-Conde et al. (2008). We stacked the 24 μm simulated sources per flux bin in the BLAST simulated maps. We measured the mean BLAST flux for each 24 μm bin with the same method as applied on the real data. At the same time we computed the mean sub-mm flux for the same selection from the mock catalog associated to the simulation. We finally compared the mean BLAST fluxes measured by stacking with those directly derived from the mock catalog to estimate the possible biases (see Fig. 5). The stacking measurements and expected values agree within the error bars. We notice a weak trend of overestimation of the stacked fluxes at low flux density (S_{24} < 200 μJy) however, but it is still within the error bars. We can thus stack 24 μm *Spitzer* sources in the BLAST map.

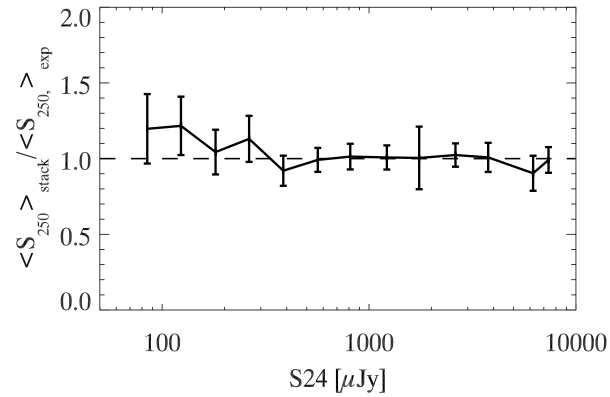

Fig. 5. Ratio between the mean flux density at 250 μm found by the stacking analysis and the expected flux for different S_{24} bins. It is based on a Fernandez-Conde et al. (2008) simulation of a 0.25 deg^2 field with a noise and PSF similar to the BLAST deep region.

5.3. Mean 24 μm to sub-mm color deduced by stacking analysis

The stacking analysis allowed to measure the mean 24 μm to sub-mm colors of undetected sub-mm galaxies. These colors depends on the SED of galaxies (or K-correction) and the redshift distribution in a degenerate way. The $S_{\mathrm{submm}}/S_{24}$ color and $\mathrm{d}S_{\mathrm{submm}}/\mathrm{d}S_{24}$ as a function of S_{24} are plotted in Fig. 6.

The colors are higher for the fainter 24 μm flux (S_{24} < 100 μJy). This behavior agrees with the model expectations: the faint sources at 24 μm lie at a higher mean redshift than the brighter ones. Due to the K-correction, the high-redshift sources have a brighter sub-mm/24 color than local ones.

The colors found by the stacking analysis are lower than those obtained by an extraction at 250 μm (Sect. 4.5). It is an effect of selection. The mid-infrared is less affected by the K-correction than the sub-mm, and a selection at this wavelength selects lower redshift objects. We thus see lower colors because of the position of the SED peak (around 100 μm restframe).

We also investigated the evolution of the derivative $\mathrm{d}S_{\mathrm{submm}}/\mathrm{d}S_{24}$ as a function of S_{24}, which explicits how the observed sub-mm flux increases with the 24 μm flux densities. At high 24 μm flux densities (S_{24} > 400 μJy) the derivative is almost constant and small (<20 and compatible with zero), meaning that the observed sub-mm flux density does not vary much with S_{24}. For these flux bins we select only local sources and do not expect a strong evolution of the color. At fainter 24 μm flux densities the observed decrease can be explained by redshift and K-correction effects, as above.

The color in the faintest 24 μm flux density bin (70 to 102 μJy) is slightly fainter than in the neighboring points. It can be due to the slight incompleteness of the 24 μm catalog (about 15%), which varies spatially across the field: the sources close to the brightest sources at 24 μm are hardly extracted. The consequence is a bias to the lower surface density regions, leading to a slight underestimation of the stacked flux measurement.

5.4. Accuracy of the stacking counts method on BLAST with a Spitzer 24 μm prior

Béthermin et al. (2010) showed that the stacking counts could be biased: the color of sources can vary a lot as a function of the redshift. The assumption of a single color for a given S_{24}

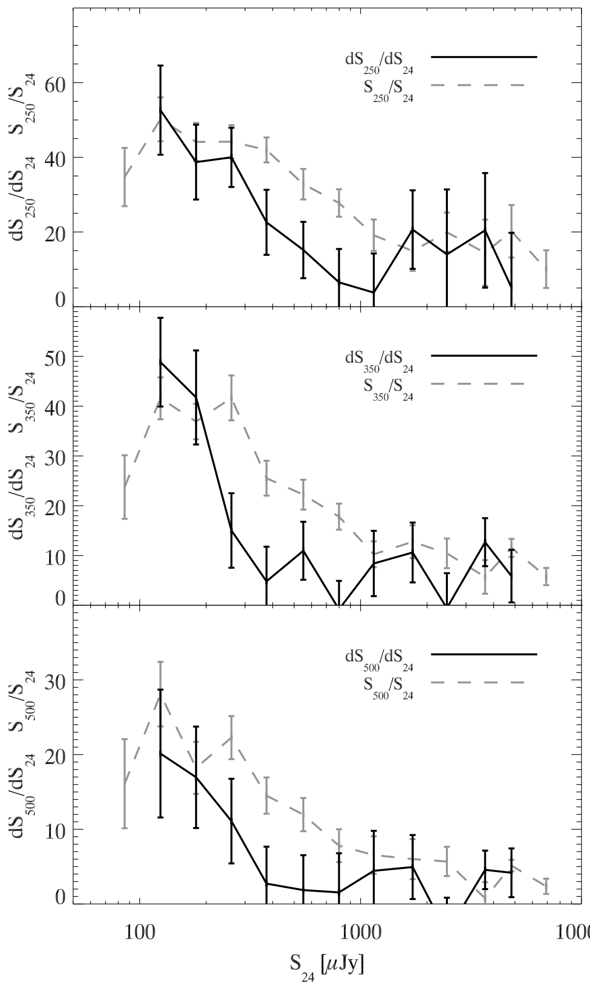

Fig. 6. *Black solid line*: $dS_{\rm submm}/dS_{24}$ as a function of S_{24}. *Grey dashed line*: $S_{\rm submm}/S_{24}$ color as a function of S_{24}.

is not totally realistic and explains some biases. We used two simulated catalogs (containing for each source S_{24}, S_{250}, S_{350} and S_{500}) to estimate this effect: a first one based on the Lagache et al. (2004) model that covered 20×2.9 deg^2 and a second one based on the Le Borgne et al. (2009) model and that covered 10 deg^2. The large size of these simulations allows us to neglect cosmic variance.

In order to compute the stacking counts, we first computed the counts at 24 μm from the mock catalog. Then we computed the mean $S_{250,\,350\,or\,500}$ flux density (directly in the catalog) in several S_{24} bins to simulate a stacking. We finally applied the Eq. (7) to compute stacking counts at the BLAST wavelengths.

The ratio between the stacking counts and the initial counts is plotted in Fig. 8 for the two mock catalogs. Between 1 mJy and 10 mJy we observe an oscillating bias. This bias is less than 30% at 250 μm and 50% at other wavelengths. When the flux becomes brighter than 25 mJy at 250 μm (18 mJy at 350 μm and 7.5 mJy at 350 μm), we begin to strongly underestimate the counts. The analysis of real data also shows a very strong decrease in the counts around the same fluxes (see Fig. 7). Consequently, we cut our stacking analysis at these fluxes and we applied an additional uncertainty to the stacking counts of 30% at 250 μm (50% at 350 μm and 500 μm).

Using the 24 μm observations as a prior to stack in the BLAST bands seems to give less accurate results than in the *Spitzer* MIPS bands. For a given S_{24} flux, the sub-mm emission can vary a lot as a function of the redshift. But the simulations shows that this method works for faint flux densities. It is due to the redshift selection which is similar for faint flux densities (see Fig. 9) and very different at higher flux densities (see Fig. 10). For example, $S_{24} \sim 100$ μJy sources are distributed around $z = 1.5$ with a broad dispersion in redshift. $S_{350} \sim 4$ mJy (based on averaged colors, 4 mJy at 350 μm corresponds to $S_{24} \sim 100$ μJy) sources have quite a similar redshift distribution except an excess for $z > 2.6$. At higher flux densities (around 2 mJy at 24 μm) the distribution is very different. The majority of the 24 μm-selected sources lies at $z < 1$ and the distribution of 350 μm-selected sources peaks at $z \sim 1.5$. Another possible explanation is that fainter sources lies near $z = 1$ and are thus selected at the 12 μm rest-frame, which is a very good estimator of the infrared bolometric luminosity according to Spinoglio et al. (1995).

In order to limit the scatter of the sub-mm/24 color, we tried to cut our sample into two redshift boxes following the Devlin et al. (2009) IRAC color criterion ([3.6]–[4.5] = 0.068([5.8]–[8.0])–0.075). But we had not enough signal in the stacked images to perform the analysis.

6. Interpretation

6.1. Contribution to the CIB

We integrated our counts assuming power-law behavior between our points. Our points are not independent (especially the stacking counts), and we thus combined errors linearly. The contribution of the individually detected sources ($S_{250} > 64$ mJy, $S_{350} > 54$ mJy, $S_{500} > 49$ mJy) is then $0.24^{+0.18}_{-0.13}$ nW.m^2.sr^{-1}, $0.06^{+0.05}_{-0.04}$ nW.m^2.sr^{-1} and $0.01^{+0.01}_{-0.01}$ nW.m^2.sr^{-1} at 250 μm, 350 μm and 500 μm, respectively. Considering the total CIB level of Fixsen et al. (1998) (FIRAS absolute measurement), we resolved directly only 2.3%, 1.1% and 0.4% at 250 μm, 350 μm and 500 μm, respectively.

The populations probed by the stacking counts ($S_{250} > 6.2$ mJy, $S_{350} > 5.2$ mJy, $S_{500} > 3.5$ mJy) emit $5.0^{+2.5}_{-2.6}$ nW m^2 sr^{-1}, $2.8^{+1.8}_{-2.0}$ nW m^2 sr^{-1} and $1.4^{+2.1}_{-1.3}$ nW m^2 sr^{-1} at 250 μm, 350 μm and 500 μm, respectively. This corresponds to about 50% of the CIB at these three wavelengths.

6.2. Comparison with Patanchon et al. (2009)

The agreement between our resolved counts built from the catalogs and the P(D) analysis of Patanchon et al. (2009) is excellent (Fig. 2). We confirm the efficiency of the P(D) analysis to recover number counts without extracting sources. The stacking counts probe the flux densities between 6 mJy and 25 mJy at 250 μm (between 5 mJy and 13 mJy at 350 μm and 3 mJy and 7 mJy at 500 μm). In this range there is only one P(D) point. At the three BLAST wavelengths the P(D) points agree with our stacking counts (Fig. 2). Our results thus confirm the measurement of Patanchon et al. (2009) and give a better sampling in flux.

6.3. Comparison with ground-based observations

We compared our results with sub-mm ground-based observations of SHARC. Khan et al. (2007) estimated a density of $S_{350} > 13$ mJy sources of $0.84^{+1.39}_{-0.61}$ arcmin^{-2}. For the same cut,

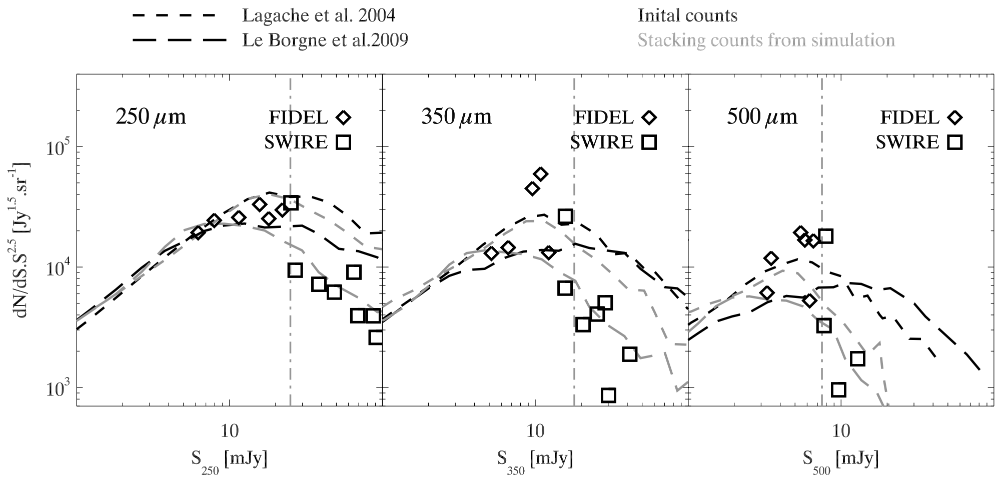

Fig. 7. Number counts at BLAST wavelengths coming from the data (*points*) and the models (*lines*). *Short dashed line*: initial *(black)* and stacking *(grey)* counts from the Lagache et al. (2004) mock catalog; *long dashed line*: initial *(black)* and stacking *(grey)* counts from Le Borgne et al. (2009); *diamond*: stacking counts built with the FIDEL catalog; *square*: stacking counts built with the SWIRE catalog; *grey vertical dot-dash line*: flux cut for stacking counts.

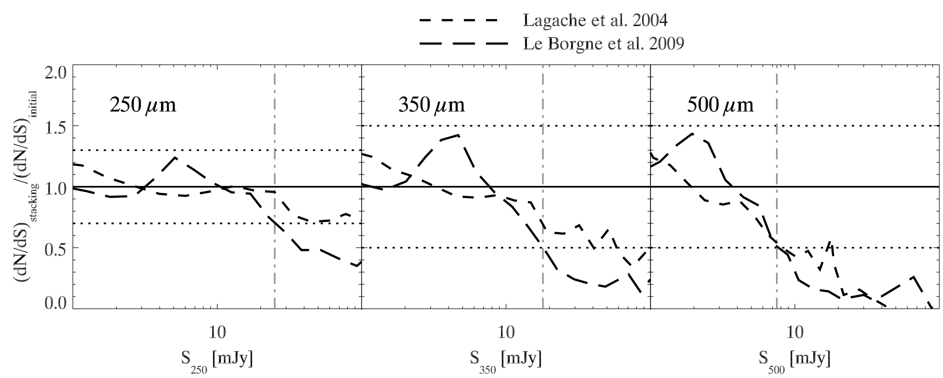

Fig. 8. Ratio between stacking counts and initial counts for two mock catalogs; *short dashed line*: Lagache et al. (2004) catalog; *long dashed line*: Le Borgne et al. (2009); *grey vertical dot-dash line*: flux cut for stacking counts; *horizontal dot line*: estimation of the uncertainty intrinsic to the stacking method.

we found 0.26 ± 0.13 arcmin^{-1}, which agrees with their work. Our measurement (175 ± 75 sources deg^{-2} brighter than 25 mJy) agrees also with that of Coppin et al. (2008) ones at the same wavelength (200–500 sources deg^{-2} brighter than 25 mJy).

We also compared our results at 500 μm with the SCUBA ones at 450 μm. Borys et al. (2003) find 140^{+140}_{-90} gal deg^{-2} for $S_{450} > 100$ mJy. We found 1.2 ± 1.0 gal.deg^{-2}. We significantly disagree with them. Borys et al. (2003) claim 5 4-σ detections in a 0.046 deg^2 field in the *Hubble* deep field north (HDFN). These five sources are brighter than 100 mJy. We find no source brighter than 100 mJy in a 0.45 deg^2 field at 350 μm nor at 500 μm. The cosmic variance alone thus cannot explain this difference. A possible explanation is that they underestimated the noise level and their detections are dominated by spurious sources. It could also be due to a calibration shift (by more than a factor 2). The observation of the HDFN by *Herschel* will allow us to determine whether that these bright sources might be spurious detections.

We also compared our results with the estimations based on lensed sources at 450 μm with SCUBA (Smail et al. 2002; Knudsen et al. 2006). For example, Knudsen et al. (2006) find 2000–50 000 sources deg^2 brighter than 6 mJy. It agrees with our 3500^{+7700}_{-3400} sources deg^2.

6.4. Comparison with the Lagache et al. (2004) and Le Borgne et al. (2009) models

At 250 μm and 350 μm the measured resolved source counts are significantly lower (by about a factor of 2) than the Lagache et al. (2004) and Le Borgne et al. (2009) models. Nevertheless, our counts are within the confidence area of Le Borgne et al. (2009). The same effect (models overestimating the counts) was observed at 160 μm (Frayer et al. 2009; Béthermin et al. 2010). It indicates that the galaxies' SED or the luminosity functions used in both models might have to be revisited. At 500 μm our counts and both models agree very well, but our uncertainties are large, which renders any discrimination difficult.

Concerning the stacking counts, they agree very well with the two models. Nevertheless, our uncertainties are larger than 30%. We thus cannot check if the disagreement observed between the Lagache et al. (2004) model and the stacking counts at 160 μm (Béthermin et al. 2010) of 30% at $S_{160} = 20$ mJy still holds at 250 μm.

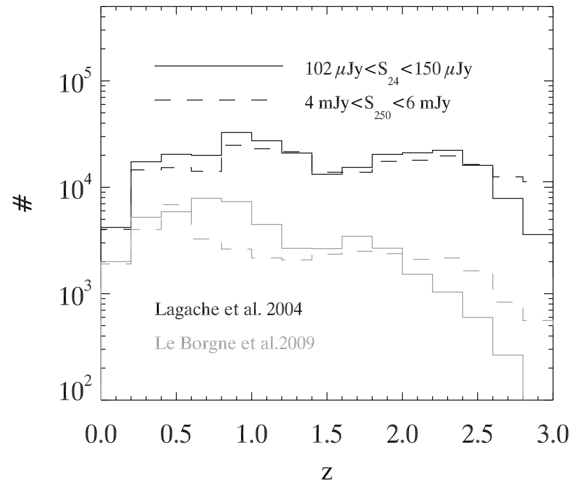

Fig. 9. *Solid line*: distribution in redshift of the sources with 102 μJy < S_{24} < 150 μJy for the mock catalogs generated with the Lagache et al. (2004) (*black*) and the Le Borgne et al. (2009) (*grey*) models; *dashed line*: distribution in redshift of the sources with 4 mJy < S_{250} < 6 mJy (determined using the mean 250/24 color).

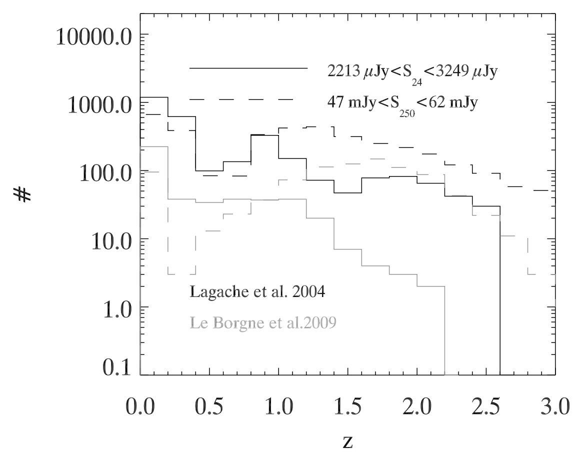

Fig. 10. *Solid line*: distribution in redshift of the sources with 2213 μJy < S_{24} < 3249 μJy for the mock catalogs generated with the Lagache et al. (2004) (*black*) and Le Borgne et al. (2009) (*grey*) models; *dashed line*: distribution in redshift of sources with 47 mJy < S_{250} < 62 mJy (determined using the mean 250/24 color).

6.5. Implications for the probed populations and the models

We showed that the two models nicely reproduce the sub-mm counts, especially below 100 mJy. We can thus use them to estimate which populations are constrained by our counts. For each flux density bin we computed the mean redshift of the selected galaxies in both models. We then used the SEDs given by the models at that mean redshift and at that flux bin and derived the infrared bolometric luminosity. The luminosities are shown in dashed lines in Fig. 11 for 350 μm as an example, and the redshift is given in solid lines.

The stacking counts reach 6.2 mJy, 5.3 mJy and 3.5 mJy at 250 μm, 350 μm and 500 μm, respectively. This corresponds to faint ULIRGs ($L_{\rm IR} \approx 1.5 \times 10^{12}\ L_\odot$) around z = 1.5, 1.8 and 2.1 at 250 μm, 350 μm and 500 μm, respectively. Our measurements show that the predicted cold-dust emissions (between 100 μm

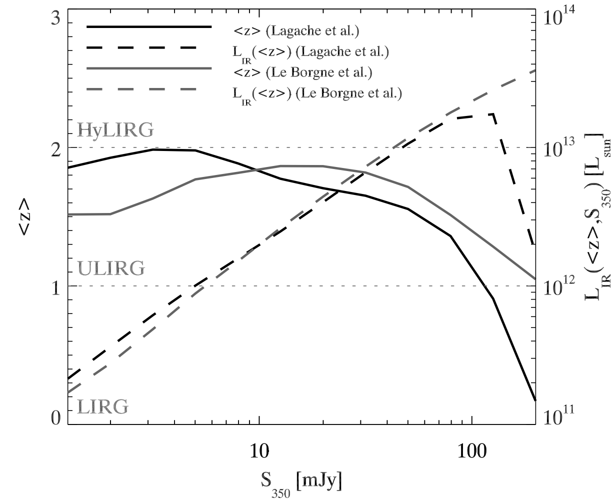

Fig. 11. Mean redshift (*solid line*) of sources for different fluxes at 350 μm for the Lagache et al. (2004) (*black*) and Le Borgne et al. (2009) (*grey*) models and corresponding infrared luminosity defined in Sect. 6.5 (*dashed line*).

and 200 μm rest frame) of this population in the models are believable.

At 250 μm and 350 μm the resolved sources (S_{350} > 85 mJy) are essentially $z \sim 1$ ULIRGs ($L_{\rm IR} > 10^{12} L_\odot$) and HyLIRGs ($L_{\rm IR} > 10^{13}\ L_\odot$) according to the models. In Lagache et al. (2004) the local cold-dust sources contribute at very bright flux (>200 mJy). This population is not present in the Le Borgne et al. (2009) model. It explains the difference between the two models for fluxes brighter than 100 mJy at 350 μm (see Fig. 11). At 500 μm, Lagache et al. (2004) predict that bright counts are dominated by local cold-dust populations and Le Borgne et al. (2009) that they are dominated by medium redshift HyLIRGs. Nevertheless, there is a disagreement with the observations for this flux density range, suggesting that there could be less HyLIRGs than predicted. But these models do not currently include any AGN contribution, which is small except at luminosities higher than $10^{12}\ L_\odot$ (Lacy et al. 2004; Daddi et al. 2007; Valiante et al. 2009).

7. Conclusion

Our analysis provides new stacking counts, which can be compared with the Patanchon et al. (2009) P(D) analysis. We have a good agreement between the different methods. Nevertheless, some methods are more efficient in a given flux range.

The blind extraction and the extraction using a prior give a better sampling in flux and slightly smaller error bars. The P(D) analysis uses only the pixel histogram and thus looses the information on the shape of the sources. The blind extraction is a very efficient method for extracting the sources, but lots of corrections must be applied carefully. When the confusion noise totally dominates the instrumental noise, the former must be determined accurately, and the catalog flux limit must take this noise (Dole et al. 2003) into account.

Estimating the counts from a catalog built using a prior is a good way to deal with the flux boosting effect. This method is based on assumptions however. We assume that all sources brighter than the flux cut at the studied wavelength are present in the catalog extracted using a prior. We also assume a flux distribution at the studied wavelength for a selection at the prior wavelength to correct for the Eddington bias. Consequently an extraction using a prior must be used in a flux range where the blind extraction is too affected by the flux boosting to be accurately corrected.

P(D) analysis and stacking counts estimate the counts at flux densities below the detection limit. These methods have different advantages. The P(D) analysis fits all the fluxes at the same time, where the stacking analysis flux depth depends on the prior catalog's depth (24 μm *Spitzer* for example). But the P(D) analysis with a broken power-law model is dependent on the number and the positions of the flux nodes. The uncertainty due to the parameterization was not evaluated by Patanchon et al. (2009). The stacking counts on the other hand are affected by biases due to the color dispersion of the sources. The more the prior and stacked wavelength are correlated, the less biased are the counts. A way to overcome this bias would be to use a selection of sources (in redshift slices for example), which would reduce the color dispersion, and the induced bias; we did not use this approach here because of a low signal-to-noise ratio.

The stacking and P(D) analysis are both affected by the clustering in different ways. For the stacking analysis this effect depends on the size of the PSF. This effect is small for BLAST and will be smaller for SPIRE. The clustering broadens the pixel histogram. Patanchon et al. (2009) show that it is negligible for BLAST. Clustering will probably be an issue for SPIRE. The cirrus can also affect the P(D) analysis and broaden the peak. Patanchon et al. (2009) use a high-pass filtering that reduces the influence of these large scale structures.

The methods used in this paper will probably be useful to perform the analysis of the *Herschel* SPIRE data. The very high sensitivity and the large area covered will reduce the uncertainties and increase the depth of the resolved source counts. Nevertheless, according to the models (e.g. Le Borgne et al. (2009)), the data will also be quickly confusion-limited and it will be very hard to directly probe the break of the counts. The P(D) analysis of the deepest SPIRE fields will allow us to constrain a model with more flux nodes and to better sample the peak of the normalized differential number counts. The instrumental and confusion noise will be lower, and a stacking analysis per redshift slice will probably be possible. These analyses will give stringent constraints on the model of galaxies and finally on the evolution of the infrared galaxies.

Acknowledgements. We warmly acknowledge Guillaume Patanchon for his precious comments and discussions. We thank Damien Le Borgne and Guilaine Lagache for distributing their model and their comments. We also acknowledge Alexandre Beelen and Emeric Le Floc'h for their useful comments. We thank Maxime Follin, for his help during his Licence 3 training at the Université Paris Sud 11. We thank the BLAST team for the well-documented public release of their data. We warmly thank the referee Steve Willner, who helped a lot to improve the quality of this paper. This work is based in part on archival data obtained with the Spitzer Space Telescope, which is operated by the Jet Propulsion Laboratory, California Institute of Technology under a contract with NASA. Support for this work was provided by an award issued by JPL/Caltech.

Appendix A: Effect of clustering on the uncertainties of number counts

Béthermin et al. (2010) showed how the clustering is linked with the uncertainties of the counts. We used the formalism of Béthermin et al. (2010) to estimate the effect of the clustering on our BLAST counts. There are few sources detected at 250 μm and the BLAST coverage is inhomogeneous. It is consequently very hard to estimate the clustering of the resolved population. We thus used the clustering measured at 160 μm by Béthermin et al. (2010) and assumed a 250/160 color equal to unity. We then used the same method to compute the uncertainties. We then compare the uncertainties with and without clustering. Neglecting the clustering implies an underestimation of the uncertainties on the counts of 35% in the 203–336 mJy bin at 250 μm, and less than 20% in the other bins. We can thus suppose a Poissonian behavior, knowing that the Poisson approximation underestimates the error bars for the 203–336 mJy bin at 250 μm. Nevertheless, our model of clustering at 250 μm has strong assumptions (single 250/160 color, same clustering at 250 μm as measured at 160 μm), and it would be more conservative to update it with *Herschel* clustering measurements.

Appendix B: Effect of clustering on stacking

B.1. A formalism to link clustering and stacking

The clustering can bias the results of a stacking. We present a formalism based on Bavouzet (2008) work.

The expected results for mean stacking of an N non-clustered populations is

$$M(\theta) = \overline{S_s} \times PSF(\theta) + \int_0^\infty S \frac{dN}{dS} dS, \tag{B.1}$$

where M is the map resulting from stacking, θ the distance to the center of the cutout image, $\overline{S_s}$ the mean flux of the stacked population. The integral is an approximation because the central source is treated in the first term. This approximation is totally justified in a strongly confused field where the number of sources is enormous. PSF is the instrumental response and is supposed to be invariant per rotation ($\theta = 0$ corresponds to the center of this PSF). $\frac{dN}{dS}$ is the number of the source per flux unit and per pixel. We assume an absolute calibration. The integral in the Eq. (B.1) is equal to the CIB brightness

$$I_{\mathrm{CIB}} = \int_0^\infty S \frac{dN}{dS} dS. \tag{B.2}$$

This term is constant for all pixels of the image and corresponds to a homogeneous background.

The stacked sources can actually be autocorrelated. The probability density to find a stacked source in a given pixel and another in a second pixel separated by an angle θ ($p(\theta)$) is linked with the angular autocorrelation function ($\omega(\theta)$) by

$$p(\theta) = \rho_s^2 (1 + \omega(\theta)), \tag{B.3}$$

where ρ_s is the number density of the stacked source.

If we assume that there is no correlation with other populations, the results of the stacking of N autocorrelated sources is

$$M(\theta) = \overline{S_s} \times PSF(\theta) + I_{\mathrm{CIB,s}}(1 + \omega(\theta)) * PSF(\theta) + I_{\mathrm{CIB,ns}}, \tag{B.4}$$

where $I_{\mathrm{CIB,s}}$ and $I_{\mathrm{CIB,ns}}$ is the CIB contribution of stacked and non-stacked sources. If we subtract the constant background of the image, we find

$$M(\theta) = \overline{S_s} \times PSF(\theta) + I_{\mathrm{CIB,s}} \times \omega(\theta) * PSF(\theta). \tag{B.5}$$

The second term of this equation corresponds to an excess of flux due to clustering. This signal is stronger in the center of the stacked image. The central source appears thus brighter than expected, because of the contribution due to clustering.

The flux of the central stacked source computed by PSF-fitting photometry is

$$S_{\rm mes} = \frac{\int\int M \times PSF {\rm d}\Omega}{\int\int PSF^2 {\rm d}\Omega} = \overline{S_{\rm s}} + S_{\rm clus}, \tag{B.6}$$

where $S_{\rm clus}$, the overestimation of flux due to clustering is given by

$$S_{\rm clus} = I_{\rm CIB,s} \times \frac{\int\int \big((\omega * PSF) \times PSF\big) {\rm d}\Omega}{\int\int PSF^2 {\rm d}\Omega} \cdot \tag{B.7}$$

Basically, the stronger the clustering, the larger the bias. In addition, the wider the PSF, the larger the overestimation. The stacked signal can be dominated by the clustering, if the angular resolution of the instrument is low compared to the surface density of the sources (like *Planck*, cf. Fernandez-Conde et al. (2010)) or if strongly clustered populations are stacked.

B.2. Estimation of the bias due to clustering

The estimation of $S_{\rm clus}$ with Eq. (B.7) requires particular hypotheses. The stacked population is $S_{24} > 70$ μJy sources detected by *Spitzer*. Their contribution to the CIB is 5.8 nW m^{-2} sr^{-1}, 3.4 nW m^{-2} sr^{-1} and 1.4 nW m^{-2} sr^{-1} at 250 μm, 350 μm and 500 μm, respectively (estimated by direct stacking of all the sources). Following the clustering of 24 μm sources estimated by Béthermin et al. (2010), we suppose the following autocorrelation function:

$$\omega(\theta) = 2.3 \times 10^{-4} \times \left(\frac{\theta}{\rm deg}\right)^{-0.8} \cdot \tag{B.8}$$

The excess of flux due to clustering ($S_{\rm clus}$) is then 0.44 mJy, 0.35 mJy and 0.16 mJy at 250 μm, 350 μm and 500 μm, respectively. This is significantly lower than the bootstrap uncertainties on these fluxes. We can thus neglect the clustering.

B.3. Measurement of the angular correlation function by stacking

This new formalism provides a simple tool to measure the angular autocorrelation function (ACF) from a source catalog. This method uses a map called "density map". One pixel of this map contains the number of sources centered on it. It is equivalent of a map of unit flux sources with the $PSF = \delta$ (Dirac distribution). The result of the stacking is thus

$$M(\theta) = \rho_{\rm s} \times \delta(\theta) + \rho_{\rm s}(1 + \omega(\theta)). \tag{B.9}$$

The ACF can then be easily computed with

$$\forall \theta \neq 0, \omega(\theta) = \frac{M(\theta)}{\rho_{\rm s}} - 1. \tag{B.10}$$

References

Ashby, M. L. N., Stern, D., Brodwin, M., et al. 2009, ApJ, 701, 428
Barmby, P., Huang, J., Ashby, M. L. N., et al. 2008, ApJS, 177, 431
Bavouzet, N. 2008, Ph.D. Thesis, Université Paris-Sud 11 http://tel.archives-ouvertes.fr/tel-00363975/
Beelen, A., Cox, P., Benford, D. J., et al. 2006, ApJ, 642, 694
Benford, D. J., Cox, P., Omont, A., Phillips, T. G., & McMahon, R. G. 1999, ApJ, 518, L65
Bertin, E., & Arnouts, S. 1996, A&AS, 117, 393
Béthermin, M., Dole, H., Beelen, A., et al. 2010, A&A, 512, A78
Borys, C., Chapman, S., Halpern, M., et al. 2003, MNRAS, 344, 385
Chapman, S. C., Blain, A. W., Ivison, R. J., et al. 2003a, Nature, 422, 695
Chapman, S. C., Helou, G., Lewis, G. F., et al. 2003b, ApJ, 588, 186
Chapman, S. C., Blain, A. W., Smail, I., et al. 2005, ApJ, 622, 772
Chary, R., & Elbaz, D. 2001, ApJ, 556, 562
Chary, R., Casertano, S., Dickinson, M. E., et al. 2004, ApJS, 154, 80
Coppin, K., Halpern, M., Scott, D., et al. 2008, MNRAS, 384, 1597
Daddi, E., Alexander, D. M., Dickinson, M., et al. 2007, ApJ, 670, 173
Devlin, M. J., Ade, P. A. R., Aretxaga, I., et al. 2009, Nature, 458, 737
Dole, H., Gispert, R., Lagache, G., et al. 2001, A&A, 372, 364
Dole, H., Lagache, G., & Puget, J.-L. 2003, ApJ, 585, 617
Dole, H., Le Floc'h, E., Pérez-González, P. G., et al. 2004, ApJS, 154, 87
Dole, H., Lagache, G., Puget, J.-L., et al. 2006, A&A, 451, 417
Dunne, L., Eales, S., Edmunds, M., et al. 2000, MNRAS, 315, 115
Dye, S., Ade, P. A. R., Bock, J. J., et al. 2009, ApJ, 703, 285
Fazio, G. G., Ashby, M. L. N., Barmby, P., et al. 2004a, ApJS, 154, 39
Fazio, G. G., Hora, J. L., Allen, L. E., et al. 2004b, ApJS, 154, 10
Fernandez-Conde, N., Lagache, G., Puget, J.-L., et al. 2008, A&A, 481, 885
Fernandez-Conde, N., Lagache, G., Puget, J.-L., et al. 2010, A&A, 515, A48
Fixsen, D. J., Dwek, E., Mather, J. C., Bennett, C. L., & Shafer, R. A. 1998, ApJ, 508, 123
Franceschini, A., Rodighiero, G., Cassata, P., et al. 2006, A&A, 453, 397
Franceschini, A., Rodighiero, G., Vaccari, M., Marchetti, L., & Mainetti, G. 2009, A&A, accepted [arXiv:0906.4264]
Frayer, D. T., Fadda, D., Yan, L., et al. 2006a, AJ, 131, 250
Frayer, D. T., Huynh, M. T., Chary, R., et al. 2006b, ApJ, 647, L9
Frayer, D. T., Sanders, D. B., Surace, J. A., et al. 2009, AJ, 138, 1261
Gispert, R., Lagache, G., & Puget, J. L. 2000, A&A, 360, 1
Gruppioni, C., Pozzi, F., Lari, C., Oliver, S., & Rodighiero, G. 2005, ApJ, 618, L9
Hauser, M. G., & Dwek, E. 2001, ARA&A, 39, 249
Hauser, M. G., Arendt, R. G., Kelsall, T., et al. 1998, ApJ, 508, 25
Ivison, R. J., Greve, T. R., Smail, I., et al. 2002, MNRAS, 337, 1
Ivison, R. J., Smail, I., Dunlop, J. S., et al. 2005, MNRAS, 364, 1025
Kashlinsky, A. 2005, Phys. Rep., 409, 361
Khan, S. A., Chanial, P. F., Willner, S. P., et al. 2009, ApJ, 706, 319
Khan, S. A., Shafer, R. A., Serjeant, S., et al. 2007, ApJ, 665, 973
Knudsen, K. K., Barnard, V. E., van der Werf, P. P., et al. 2006, MNRAS, 368, 487
Kovács, A., Chapman, S. C., Dowell, C. D., et al. 2006, ApJ, 650, 592
Lacy, M., Storrie-Lombardi, L. J., Sajina, A., et al. 2004, ApJS, 154, 166
Lagache, G., Abergel, A., Boulanger, F., Désert, F. X., & Puget, J.-L. 1999, A&A, 344, 322
Lagache, G., Dole, H., Puget, J.-L., et al. 2004, ApJS, 154, 112
Lagache, G., Puget, J.-L., & Dole, H. 2005, ARA&A, 43, 727
Le Borgne, D., Elbaz, D., Ocvirk, P., et al. 2009, A&A, 504, 727
LeFloc'h, E., Aussel, H., Ilbert, O., et al. 2009, ApJ, 703, 222
Lewis, G. F., Chapman, S. C., & Helou, G. 2005, ApJ, 621, 32
Magdis, G. E., Rigopoulou, D., Huang, J., et al. 2008, MNRAS, 386, 11
Marleau, F. R., Fadda, D., Storrie-Lombardi, L. J., et al. 2004, ApJS, 154, 66
Marsden, G., Ade, P. A. R., Bock, J. J., et al. 2009, ApJ, 707, 1729
Michałowski, M. J., Hjorth, J., & Watson, D. 2010, A&A, 514, A67
Papovich, C., Dole, H., Egami, E., et al. 2004, ApJS, 154, 70
Pascale, E., Ade, P. A. R., Bock, J. J., et al. 2008, ApJ, 681, 400
Patanchon, G., Ade, P. A. R., Bock, J. J., et al. 2008, ApJ, 681, 708
Patanchon, G., Ade, P. A. R., Bock, J. J., et al. 2009, ApJ, 707, 1750
Pearson, C., & Khan, S. A. 2009, MNRAS, 399, L11
Pope, A., Borys, C., Scott, D., et al. 2005, MNRAS, 358, 149
Pope, A., Scott, D., Dickinson, M., et al. 2006, MNRAS, 370, 1185
Puget, J.-L., Abergel, A., Bernard, J.-P., et al. 1996, A&A, 308, L5
Rieke, G. H., Young, E. T., Engelbracht, C. W., et al. 2004, ApJS, 154, 25
Rodighiero, G., Lari, C., Pozzi, F., et al. 2006, MNRAS, 371, 1891
Rowan-Robinson, M. 2009, MNRAS, 394, 117
Sajina, A., Borys, C., Chapman, S., et al. 2003, MNRAS, 343, 1365
Sajina, A., Scott, D., Dennefeld, M., et al. 2006, MNRAS, 369, 939
Shupe, D. L., Rowan-Robinson, M., Lonsdale, C. J., et al. 2008, AJ, 135, 1050
Smail, I., Ivison, R. J., Blain, A. W., et al. 2002, MNRAS, 331, 495
Spinoglio, L., Malkan, M. A., Rush, B., Carrasco, L., & Recillas-Cruz, E. 1995, ApJ, 453, 616
Starck, J. L., Aussel, H., Elbaz, D., Fadda, D., & Cesarsky, C. 1999, A&AS, 138, 365
Stetson, P. B. 1987, PASP, 99, 191
Sullivan, I., Cooray, A., Chary, R., et al. 2007, ApJ, 657, 37
Truch, M. D. P., Ade, P. A. R., Bock, J. J., et al. 2009, ApJ, 707, 1723
Valiante, E., Lutz, D., Sturm, E., Genzel, R., & Chapin, E. 2009, ApJ, 701, 1814